PAPER • OPEN ACCESS

Damage evolution in Plasma Facing Materials by a sequential multiscale approach

To cite this article: G. Lo Presti and A. La Magna 2024 *Nucl. Fusion* **64** 106051

OPEN ACCESS
IOP Publishing | International Atomic Energy Agency
Nuclear Fusion
Nucl. Fusion **64** (2024) 106051 (22pp)
https://doi.org/10.1088/1741-4326/ad6ba6

Damage evolution in Plasma Facing Materials by a sequential multiscale approach

G. Lo Presti[1,2,*] **and A. La Magna**[2]

[1] Dipartimento di Fisica e Astronomia 'Ettore Majorana', Universitá degli Studi di Catania, Via S. Sofia, 64, 95123 Catania CT, Italy
[2] CNR IMM, Z.I. VIII Strada 5, 95121 Catania, Italy

E-mail: giorgio.lopresti@dfa.unict.it

Received 23 February 2024, revised 8 July 2024
Accepted for publication 6 August 2024
Published 9 September 2024

Abstract

Describing the time evolution of Plasma Facing Materials (PFMs), through quantitative evaluations of erosion, roughness, and physical properties degradation, is one of the difficult challenges to reach the goal of efficient energy production by nuclear fusion. To follow all the aging-connected physical and chemical phenomena through their characteristic dimensional scale, and to estimate the PFM microstructural transformation over time, we propose a predictive sequential multiscale methodology, consisting of two database-provided coupled codes. The first is a time-dependent, volume-averaged, plasma simulator which describes completely this system in terms of thermodynamics, composition and evaluation of the sheath potential. Plasma solutions are geometrically rearranged by adding surface reactions and 3D geometric features. To increase sensitivity, plasma information is provided to the second code as an initial condition. Such a code is a 3D kinetic Monte Carlo in-cell algorithm for the nano-scale erosion simulation describing the PFM interactions through an extendable set of physical phenomena, such as sticking, sputtering, ion enhanced removals and ion penetration. In this paper, we perform simulations for the case of study of Hydrogen (H) plasmas produced in linear devices, reaching the quasi-atomic detail of the plasma induced material modification of tungsten (W) as PFM.

Keywords: Plasma Facing Materials, nuclear fusion, multiscale, simulations, nuclear materials, tungsten

(Some figures may appear in colour only in the online journal)

* Author to whom any correspondence should be addressed.

Abbreviations and acronyms

He	Helium
H	Hydrogen
PFMs	Plasma Facing Materials
KMC	Kinetic Monte Carlo
W	Tungsten

1. Introduction

Increasing energy production, while reducing pollutants emissions, is one of the main aims behind the design of nuclear fusion reactors [1–4]. To guarantee the feasibility of this project, optimization of technological applications and development of new techniques are required along with various underway studies [5–7]. If we consider, for instance, the maintainability of the Deuterium-Tritium (D-T) reaction, even though progress in magnetic confinement has been made, further knowledge of dust and powder plasma contamination, plasma facing interaction, and wall aging phenomenology are needed or still under research [8–10]. Among them, our effort is concentrated on the description of plasma-wall interactions and on the consequent material evolution. In fact, different kinds of particles (in terms of mass and electric charge), depending on the plasma stoichiometry, escape from the magnetic confinement and release their energy against the reactor walls. This may happen through many physical and chemical interactions and, based on their impact energy and mutual composition, both ionic and neutral particles can interact differently on the surface or penetrate the bulk inducing a different phenomenology [11, 12]. The accumulation of wall defects is produced both by 14.06 MeV primary neutrons and by electromagnetic plasma secondary particles accelerated by the sheath potential. This can invalidate the characteristics of the entire material due to changes in its microstructure [13], and impair tritium breeding, necessary for the combustion agent re-circulation [14]. In our computational research we differentiate the contribution of these particles originated in a fusion plasma environment and follow them through their interactions with the material. The aim is the prediction of the plasma-induced Plasma Facing Material (PFM) aging, which consists in the deterioration of materials that are in direct contact with the plasma. Considering their formation processes, the correct energy distribution can be derived per each particle, and consequently the phenomena that they can induce on the material. We underline that the correlation between the plasma conditions and the surface reactions is fundamental to describe the evolution of the latter as a result of the combination of various phenomena on many energy scales.

For this reason, we employ the concept of multiscale physics, which has been already indicated as necessary by other authors for descriptive purposes (for instance Marian provided a complete review on tungsten (W) as PFM [15]) implementing it in a computational modeling framework by extending the set of phenomena that have been studied by means of simplified effective models (see e.g. Nordlund who performed a multiscale study for tokamak applications [16]). A multiscale approach is, in fact, necessary to evaluate processes which are distributed over a large set of characteristic distances, times and energies and is well suited to describe erosion processes. To practically realize our purpose, we therefore introduce a sequential multiscale computational method (which is designed to be released upon reasonable request as open-source) able to simulate the fusion plasma PFMs aging through the analysis of the evolution of the physical properties of such materials. We will divide our simulations among different codes, each one is specialized for a typical length spectrum. Precisely, this aging code will be split into the following sub-codes:

- An input code, constituted by a 0D volume-averaged plasma simulator that provides us information about the plasma characterization;
- A Monte Carlo (MC) simulator that takes into account, at the atomic resolution, nano-structural phenomena (accounting for instance sputtering, impingement, bulk penetration, and sticking).

We decided to perform plasma simulations referring to a plasma source with linear geometry, which could allow a feasible and faster experimental validation, before expanding the method to more complex configurations and aging prediction in the reactor like environment. Indeed, to measure the erosion effects on refractory materials, linear devices became very common and different facilities have been built, spanning the line in terms of features and purposes. Among them, we recall: MAGNUM-PSI [17], PSIEC [18], PMECR II [19] and GyM [20]. Studies of plasma-wall interactions on linear plasma devices are also being carried out by the EUROfusion consortium [21]. The literature provides us with several plasma characterization codes, i.e. codes that allow us to evaluate the thermodynamic parameters of the system (such as temperature and concentration). Examples in full 3D geometry include SOLPS-ITER and SOLEDGE. SOLPS-ITER is a plasma boundary code package combining a 2D multi-fluid plasma transport code [22]. SOLEDGE2D is a transport code that can be used for plasma-wall interactions simulations [23, 24]. Both codes arise from the previous EIRENE, a 3D Kinetic Monte Carlo (3D-KMC) for neutral transport, and B2, an edge plasma fluid code [25]. To simplify the computational approach, some zero-dimensional volume-averaged models have been also considered, which is especially recommended in case of linear devices. We can mention the paper by Tonello *et al* about a 0D volume-averaged approach modeling the GyM machine. In this work the authors underline the advantages of using 0D models compared to full 3D correspondents, such as SOLPS, in case of linear facilities [20]. While Tonello's work focused on Helium (He), the paper written by Samuell and Corr [26] studied hydrogen plasmas taking into account even the H_2 molecular states.

It should also be underlined that the study of plasmas in conditions similar to those generated in linear accelerators is a very popular topic in the microelectronics community. For instance, Lieberman and Lichtenberg are mainstays of the literature in such a sector [27] in which several examples of 0D plasma can be mentioned [28–30]. We decided to build up our plasma input code within this framework. It is a zero-dimensional volume-averaged database-provided plasma simulator that automatically writes and solves a set of coupled ODEs representing the thermodynamic plasma state in terms of stoichiometric concentrations, temperature, and sheath potential. In the present paper, it has been optimized to describe a hydrogen plasma with an initialization of molecular hydrogen gas flow.

The knowledge of the coupling between plasma and PFMs is fundamental both in fusion confinement environments and in the production of microelectronic devices through plasma etching. In the latter case, KMC models have already been coupled to plasma input codes to rise the sensitivity of the output [31, 32]. As regards erosion, within the scope of nuclear fusion applications, many codes are already present in the literature: for instance ERO or WallDYN. Particularly Ero [33] is a 3D MC sputtering and re-deposition code employed in both tokamak and linear geometries [34, 35], and WallDYN [36, 37] is an integrated model of impurity migration and wall dynamics based on the DIVIMP algorithm [38]. It is able to evaluate the global impurity transport and the re-deposition processes in plasma-wall interactions.

These models consider a larger scale with respect to the atomic scale physics promoting the plasma-wall interaction. To describe the nanoscale behavior of in-cell plasma-wall processes, we set up a 3D-KMC code based on a dataset of species, that uploads the plasma input conditions from the plasma simulator. It is necessary to specify the physical interactions through matrices called by the executable when needed. Such interaction matrices can be inserted in databases making the code easily extendable to add other reactions or calibrate them independently to achieve higher accuracy. Many examples are present in the literature, but they can hardly reach the atomic sensitivity with the cell elimination procedure [39]. With respect to previous 2D models [31], the 3D feature is a remarkable property. It is fundamental to validate the geometric erosion models and enhance the interplay between multiscale codes and real facilities. This kind of approach, in the case of semiconductor plasma etching modeling, has already proved to achieve the proper sensitivity [32].

In any case, in simulating the evolution of material defects, there are many MC codes that can be used in many fields of materials science by applying the necessary adaptations. Examples could be SPPARK and MulSKIPS [40, 41] which have never been applied to a nuclear fusion environment since the sequence of evolutionary events is different (see e.g. [42]). We notice that the tools described in this paper can be in principle integrated with other simulation environments especially to exploits commonalities related to input-output modes.

The presentation of this research is divided into a chapter concerning the physical and computational modeling, which considers both the plasma and the KMC codes since the separate models will be firstly presented and then connected, and a chapter reserved for simulations and their discussion. To facilitate the understanding of the sequential coupling approach, a schematic is provided (see appendix figure 10).

2. Model description

The atomic description of the processes that affect the aging caused by plasmas, thus the direct evaluation of erosion rate, penetration length and roughness, can be properly simulated by a KMC if its initialization derives from a plasma model. Thus, a plasma simulator can be coupled to a plasma-wall interaction code to increase the input sensitivity of the latter (see figurative image figure 1).

This pairing process is indeed based on the following assumption: a plasma code can be programmed to provide, depending on the initial conditions, the plasma characterization which consists in a description of its physical state through quantitative parameters (such as composition, Debye length, plasma parameter, plasma frequency and thermal speed) which depend on the state variables and on the degree of ionization. The plasma simulations can thus provide to a KMC code a more precise stoichiometric composition and energetic distribution of the particles which could be expressed in terms of their speed and angular direction if the plasma simulator admits geometric features. Therefore, we coupled our KMC atomic description to the 0D plasma simulator, in order to obtain a tool adaptable easily and with a great precision to various stoichiometries and geometries. Moreover, this setting provides a description which desire to be compliant with the experiments. In fact, our code can reproduce the environment of a generic plasma-wall test facility evaluating the parameters that can be set or measured in its typical work condition. This favors the process of benchmarking and mutual calibration with experiments, which becomes even more favorable in the case of open-source codes.

2.1. Plasma model

Here we present a versatile code characterizing the state of the plasma over time. As already stated, for the purposes of this paper, it has been optimized for linear reactors implying the choice of a cylindrical symmetry for the chamber. It is based on a volume-averaged point model integrated with an adaptive geometry surface model which are built together with the set of bulk reactions. This approximation assumes that the particles react with no space-dependent terms and the physical quantities are averaged over the whole real volume taking into account surface corrections. Such a procedure greatly simplifies the transport equations bringing the physics to depend on the balance of a modifiable set of reactions inserted through databases.

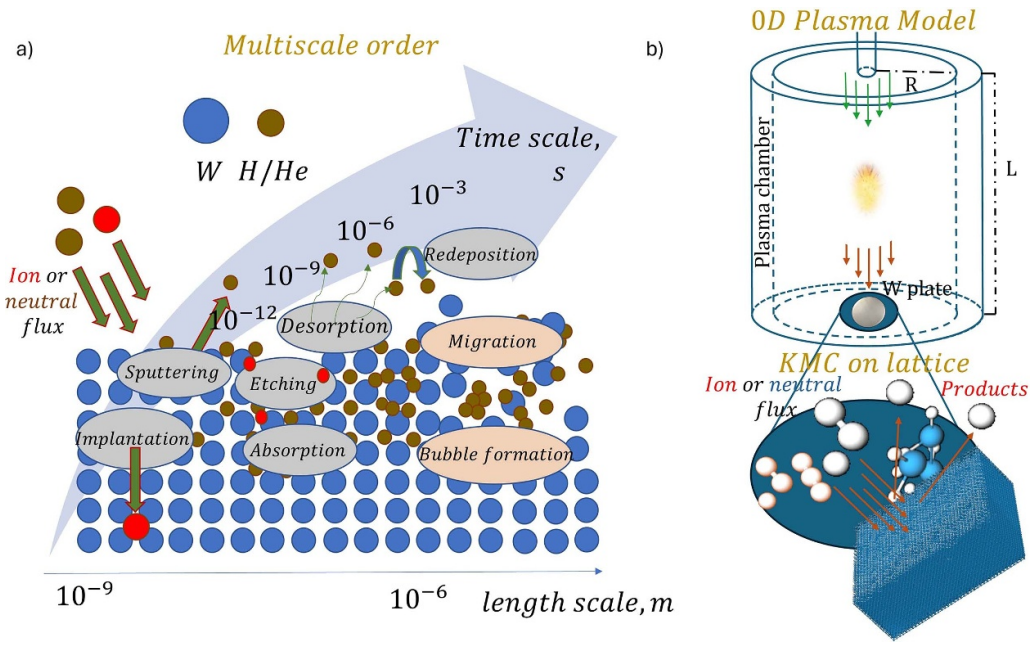

Figure 1. Figurative image of the sequential multiscale order. Panel (*a*): when particles from a plasma encounter a wall, many phenomena that trigger the aging of the wall occur simultaneously, including different scales of space and time. To simulate this process (panel (*b*), a 0D linear cylindrical plasma chamber (radius R and length L simulator, sequentially coupled with a MC tool, is used.

By model assumption, i.e. linear device, an external pumping drives gases through a cylindrical void chamber of radius R and length L. The plasma is activated by an external source and, due to the net pumping Q, flows uniformly in the chamber, except for local deviations near the walls. Moreover the distribution of electron energies is assumed to be Maxwellian.

For a complete plasma description, a set of transport equations conserving particle fluxes is imposed, coupled with the equation for energy conservation and with the plasma condition (known as 'global neutrality').

The equation set is automatically built reading the database that contains the main information for all the reactions. These models can accept different kinds of species, just adding the mutual set of reactions, and can remain stable for a wide scale in pressure and external power as verified by Lee and Lieberman [43]. The set of equations becomes the following:

$$\frac{\mathrm{d}n_\alpha}{\mathrm{d}t} = \frac{Q}{V} + \sum_j \left(R^{(\alpha)}_{\mathrm{Generation},j} - R^{(\alpha)}_{\mathrm{Loss},j}\right); \tag{1}$$

$$\frac{\mathrm{d}\left(3/2en_eT_e\right)}{\mathrm{d}t} = \frac{P}{V} - e\sum_\alpha \epsilon_c^{(\alpha)} k_{iz}^{(\alpha)} n_e n^{(\alpha)} - e\sum_{j,\mathrm{Sur}} k_{\mathrm{wall},j}\epsilon_{\mathrm{wall},j} n_j; \tag{2}$$

with the constraint:

$$n_+ = n_- + n_e, \tag{3}$$

where n_+ is the total density of positive ions ($\sum n_{\text{positive ion}}$), n_- is the corresponding for negative ones and n_e is the electronic density.

The first equation (1) describes the abundance, in terms of concentration n, of the α species over time. It is the result of the incoming flow and the balance of all the reactions in which this species is generated and lost. The reaction rate R in the j process, can be evaluated as:

$$R_j = k_j \prod_l n_{j,l}, \tag{4}$$

where k_j is the associated reaction constant tabled below (for both volume and surface reactions, see Coefficients in tables 1 and 2) and l is the reactant index for each j process.

The second equation (2) represents the energy balance. In fact, the electronic energy density $3/2en_eT_e$ (where e is the electric charge and T_e the electron temperature in eV units) changes in time due to the effect of three terms: the external power density (the external power P divided by the chamber volume V), the power acquired by volume processes, and the power required for surface reactions. These last two terms consist of sums over the energy density expressions but only in presence of electrons since only those in which electrons react can directly modify the electronic energy density.

In both terms, the sums cycle over reactions and particles. However, in the volumetric term, the summation over the processes is inherent in the definition of ϵ, and in the case of surface reactions, the interactions involving electrons occur only as binary events between the electron of the wall and each particle. In particular, ϵ_c^α is the energy lost by the particle α due to electron-impact collisions in volume and is called 'collisional energy':

Table 1. List by name, equation, rate coefficient and energy threshold of supposed volume reactions for hydrogen plasma. The reaction coefficients depend on electron temperature T_e or on the gas temperature T_g (which is the same for ions and neutrals in this version of the code) expressed in eV.

Hydrogen reactions in plasma (volume)			
Name	Reaction	Coefficients ($cm^3\ s^{-1}$)	Threshold (eV)
R1	$H_2 + e^- \rightarrow H_2^+ + e^- + e^-$	$1.10 \times 10^{-8} T_e^{0.42} e^{-16.05/T_e}$	15.43
R2	$H_2 + e^- \rightarrow H + H + e^-$	$4.73 \times 10^{-8} T_e^{-0.23} e^{-10.09/T_e}$	4.368
R3	$H_2 + e^- \rightarrow H + H^-$	$2.05 \times 10^{-11} T_e^{-1.04} e^{-9.04/T_e}$	3.750
R4	$H_2 + e^- \rightarrow H + H + e^-$	$7.89 \times 10^{-9} T_e^{0.41} e^{-14.23/T_e} v$	13.70
R5	$H + H_2^+ \rightarrow H_2 + H^+$	6.40×10^{-10}	1.000
R6	$H_2^+ + e^- \rightarrow H + H^+ + e^-$	$1.88 \times 10^{-7} T_e^{-0.39} e^{-28.82/T_e}$	0.020
R7	$H_3^+ + e^- \rightarrow H_2^+ + H^-$	$1.93 \times 10^{-10} T_e^{-1.07} e^{-2.70/T_e} +$ $+2.59 \times 10^{-9} T_e^{-1.27} e^{-6.45/(T_e+0.10)}$	0.007
R8	$H_2 + H_2^+ \rightarrow H + H_3^+$	2.00×10^{-9}	0.000
R9	$H^+ + H^- \rightarrow H + H$	$1.28 \times 10^{-7} \sqrt{300/T_g}$	0.700
R10	$H_2^+ + H^- \rightarrow H + H + H$	$8.29 \times 10^{-7} \sqrt{300/T_g}$	0.000
R11	$H_3^+ + H^- \rightarrow H + H + H + H$	$8.29 \times 10^{-7} \sqrt{300/T_g}$	0.000
R12	$H^- + e^- \rightarrow H + e^- + e^-$	$1.24 \times 10^{-6} T_e^{0.03} e^{-10.44/T_e}$	10.00
R13	$e^- + H_3^+ \rightarrow H + H + H^+ + e^-$	$1.00 \times 10^{-7} T_e^{0.37} e^{-14.46/T_e}$	15.00
R14	$H_2^+ + e^- \rightarrow H + H$	$2.35 \times 10^{-8} T_e^{0.40}$	0.010
R15	$H_2 + H^+ \rightarrow H_3^+$	1.63×10^{-15}	0.000
R16	$H_3^+ + e^- \rightarrow H + H + H$	$2.19 \times 10^{-9} T_e^{0.80}$	0.025
R17	$H_3^+ + e^- \rightarrow H + H_2$	$7.30 \times 10^{-10} T_e^{0.80}$	0.025

$$\epsilon_c^\alpha = \sum_{\text{Process}} \left(\epsilon_{\text{Process}}^\alpha \frac{k_{\text{Process}}^\alpha}{k_{iz}^\alpha} \right). \tag{5}$$

The mentioned processes in this summation will be discussed in subsections 'Volume reactions' 2.1.1 and 'Surface reactions' 2.1.2. The term ϵ_{wall} is the exchanged energy during an ion recombination. Finally, the last equation (3), i.e. the global neutrality constraint that is expected to be the plasma definition, acts as charge conservation law inside the code.

After having established the set of equations, we simulated the time evolution in the plasma with a Runge-Kutta algorithm from which we extracted the stationary solution. This choice is justified whenever the plasma reaches equilibrium before the changes it induces on the surface. However, we notice that, in a future extension, it is also possible to use the time dependent solution in a full coupled time dependent approach.

Once the plasma state has been calculated, it is possible to evaluate the energy distribution of the particles that will hit the walls. In the absence of induced electric or magnetic fields, the ions are in any case accelerated against the walls of the chamber, due to the sheath potential. Details for the calculation of this potential are given below in the subsection 'Sheath potential' 2.1.3.

2.1.1. Volume reactions. In linear plasma devices, used in material testing for fusion applications, the electronic temperature remains usually on the order of a few eV, inducing phenomena between free electrons and atoms, or between free electrons and molecules (and their related ions), or also between different molecules eventually with photoemission.

H_2 can generate a plasma with both atomic and molecular behavior, and it is more reactive than a noble gas. This implies that the corresponding set of reactions is quite complex, however it is possible to group all its reactions into subsets by simplifying the discussion (apart from the molecular ones) to imitate plasma's models of noble gasses. The molecular physics can be also taken into account to improve the sensitivity and stability of the result. For instance, Thorsteinsson's work [28], based on chlorine, also considers molecular interactions.

Among atomic processes, we can distinguish:

- ionization,
- recombination,
- excitation,
- elastic scattering,
- bremsstrahlung,
- molecular cleavage,
- dissociation,
- dissociative attachment,
- rotational excitation,
- vibrational excitation,
- excitation of molecular electronic states.

Each reaction is univocally defined by an equation accompanied by a name, a reaction coefficient and a threshold. Those are then inserted in the database (see table 1). From the tabled coefficients, we need to multiply by the concentrations of the other reactants to get the corresponding rates. Their functional approximation with temperature comes from the integral of the

process cross section σ with the Maxwellian energy distribution, according with the form:

$$k = \left(\frac{m_e}{2\pi k_b T_e}\right)^{3/2} \int_0^\infty \sigma(\nu)\, \nu e^{\frac{-m_e \nu^2}{2k_b T_e}} 4\pi \nu^2 \, \mathrm{d}\nu; \tag{6}$$

where k_b is the Boltzmann constant [44]. This is a procedure widely used in the literature, in fact the cross sections are extracted from experiments and provided in parametric form with energy [45–47]. It is preferable to calculate these functional forms and tabulate them before running the code because, once the shape of the coefficients has been estimated, no redundant calculation of the same integrals is needed while running the simulations.

2.1.2. Surface reactions. Expanding a 0D model to a 3D one provides a more realistic physical descriptions and is necessary to realize the coupling between the plasma and the walls. In case of suitable symmetries, to endow our model with geometric features, we followed substantially three operations [48, 49]: solving a system of transport laws in terms of effective area, imposing boundary conditions, and adding the surface reactions (the rates of which depend on the geometric characteristics). Indeed, the choice of surface reactions set is based on the chemistry of the problem, however their dynamics depends on the geometry. In case of linear plasma devices, it is possible to follow the procedure shown by Lichtenberg, Vahedi, Lieberman and Kim [48, 50], where the plasma constraint for the two-phase plasma density is parabolic:

$$\frac{n_+}{n_{e0}} = \alpha_0 \left(1 - \frac{x^2}{l^2}\right) + 1. \tag{7}$$

In this equation $\alpha = n_-/n_e$ is the electronegativity [43], $\alpha_0 \approx (3/2)\ \alpha$ is the central electronegativity [28], and l is the distance defined at $\alpha = 0$. According to this procedure, of which we present a brief summary showing the most important passages, the complex diffusion problem can be described by a system constituted by the flux conservation law, the Boltzmann relation, the charge conservation, the positive ion diffusion equation, and the Fick's law:

$$\sum_{i=1}^{N} q_i \Phi_i = 0, \tag{8}$$

$$\frac{\nabla n_-}{n_-} = \frac{T_e}{T_i}\frac{\nabla n_e}{n_e}, \tag{9}$$

$$\sum_{i=1}^{N} q_i n_i = 0, \tag{10}$$

$$-\frac{\mathrm{d}}{\mathrm{d}x}\left(D_{a+}\frac{\mathrm{d}n_+}{\mathrm{d}x}\right) = \sum_{proc} k_{proc_{i,j}} n_i n_j, \tag{11}$$

$$\Phi_i = -D_i \nabla n_i \pm n_i \mu_i E_i. \tag{12}$$

In this system, q_i represents the charge of the i th flux of particles Φ_i inside the chamber, T_i is the temperature for a generic ion, D_a is the ambipolar diffusion coefficient provided by Thompson [51] (to be more precise, we used an adapted form for each species as explained in appendix according with Chapman theory), E is the electric field, D_s is the diffusion coefficient for the particle s and μ_s is the corresponding mobility term. This system, once the boundary is fixed, under some approximations, transforms itself into an ordinary system if this definition of effective area is applied [28, 30]:

$$A_{\mathrm{eff}} = \frac{n_{is}}{n_i}|_{\mathrm{axial}} 2\pi R^2 + \frac{n_{is}}{n_i}|_{\mathrm{radial}} 2\pi RL, \tag{13}$$

where, for n_{is}, is meant the ion density at the sheath edge while h_l and h_R are defined in literature as $\frac{n_{is}}{n_i}|_{\mathrm{axial}} = h_L$ and $\frac{n_{is}}{n_i}|_{\mathrm{radial}} = h_R$. They are given by the ansatz [30]:

$$h_{L,R} = \left[\left(\frac{h_{L,R,0}}{1+\alpha_0}\right)^2 + h_c^2\right]^{1/2}, \tag{14}$$

the details of which are given in the appendix with more information about the theory behind the surface reactions. From this solution, it is possible to obtain the form of the Bohm velocity:

$$u_B = \frac{eT_e(1+\alpha)}{M(1+\gamma\alpha)}. \tag{15}$$

The reactions on the surfaces transfer energy to the walls of the chamber, therefore, to be consistent with the geometry, it is necessary to insert the set of all and only the significant reactions that the plasma will carry out with the wall. These can be listed similarly to what was done for volumetric reactions, and can be added into the same reaction database. The surface reaction set is then tabulated (table 2). In this table the γ coefficients are set as: $\gamma_h = 0.23$ and $\gamma_Q = 1$ [30].

It is known that surface reactions also affect molecular states. The importance of them, in 0D models, was studied by Hjartarson *et al* [30]. They are summarized in reaction R19 which is the de-excitation reaction of the H_2 molecule from the state ν to $\nu - 1$.

For both molecular and atomic states, the energy transferred during the recombination reactions was set to be 7 times the electron temperature. It is a common approximation coming from the kinetics, in fact this term can be considered like the summation of other two terms: 2 T_e is the mean kinetic energy per electron lost and 5 T_e is the mean kinetic energy per ion lost modified by the electronegativity $\epsilon_i = V_p + V_s$ [28], i.e. the pre-sheath and the sheath potential respectively.

2.1.3. Sheath potential. The large difference in temperature between electrons and positive ions allows electrons to escape from the Coulomb field of the plasma medium to reach the chamber walls (and thus form an electric potential difference because the plasma consequently shows the tendency to become positive). This potential difference, evaluated at the

Table 2. List by name, equation, rate coefficient and energy threshold of supposed surface reactions for H plasma. Here V stands for chamber volume and A for chamber area. The electronic temperature must be entered in eV.

Hydrogen reactions in plasma (surface)			
Name	Reaction	Coefficients (1/s)	Threshold (eV)
R18	$H+H+\text{wall}\rightarrow H_2$	$\frac{1}{2}\times\left[\left(\Lambda^2/D_{a_{[H]}}\right)+\left(2V(2-\gamma_h)/\left(A\overline{v_{th}}_{[H]}\gamma_h\right)\right)\right]^{-1}$	$0\ T_e$
R19	$H_2(v)+\text{wall}\rightarrow H_2(v-1)$ $[v=1-14]$	$\left[\left(\Lambda^2/D_{a_{[H_2]}}\right)+\left(2V(2-\gamma_Q)/\left(A\overline{v_{th}}_{[H_2]}\gamma_Q\right)\right)\right]^{-1}$	$0\ T_e$
R20	$H^+ +\text{wall}\rightarrow H$	$u_{B_{\left[H^+\right]}}\times A_{\text{eff}\left[H^+\right]}/V$	$7\ T_e$
R21	$H_2^+ +\text{wall}\rightarrow H_2$	$u_{B_{\left[H_2^+\right]}}\times A_{\text{eff}\left[H_2^+\right]}/V$	$7\ T_e$
R22	$H_3^+ +\text{wall}\rightarrow H+H_2$	$u_{B_{\left[H_3^+\right]}}\times A_{\text{eff}\left[\text{H}_3^+\right]}/V$	$7\ T_e$

plasma sheath V_s, accelerates the positive ions and restrains the negative ones from contacting the walls. The ones which will overcome the potential will be therefore responsible for the plasma-wall interface physics causing a back-reaction that interferes with the plasma stability itself. Using the techniques present in the literature [28], we calculated the sheath potential in order to evaluate the energetic spectrum for each species that can reach the wall and consequently induce a damage. In first approximation $|V_s|$ results around 5 times the electron temperature but this ratio can increase as the electronic temperature rises. It also depends on α term, according with the formula:

$$V_s \approx \ln\left(\frac{4\overline{u_B}}{v_{th}^e}\frac{1+\alpha}{1+\alpha\left(\overline{v_{th}^-}/v_{th}^e\right)^2}\right)T_e. \tag{16}$$

2.2. Monte Carlo simulations

The particular code of our sequential approach designed for the evaluation of the evolution processes at the atomic scale is presented in this section.

The mother volume is a virtual analogous of the real material and plasma volume defined and mapped through a 3D grid. In the mother volume the physical volumes can be defined. The portion of the mother volume in which the physical volumes are inserted and affected by the physical interactions (by the simulation) is called simulation volume. The lattice is the support of the states of the simulation volume, i.e. a computational matrix in which the value of the state is assigned at each point. The physical idea is to associate each point of the simulation volume with a (unit) cell of the material crystal lattice.

Thus, the states are integer numbers associated with a point in the simulation volume that represent the physical states of the corresponding physical lattice cell. The function that associates its state to a grid point works through a matrix that assigns integer values. The vacuum state is always represented by zero but the other states depend both on the specific material and on all the interactions that can be made with the plasma MC particles. So a physical volume is defined by assigning a value other than 'void-state' to a connected group of cells. Physical volumes can be modified during code execution.

The mother volume is fixed as a 3D box. The top of the box is the first KMC-simulated surface interfacing with the plasma region from which the MC particles are emitted.

The MC particles, which must be initialized in accordance with the stoichiometry simulated by our global plasma model, are both lattice states or tracking objects, i.e. objects associated to integer numbers whose trajectory can be interpolated on the grid. When emitted in the simulation box, they can travel and eventually encounter materials (non-zero state of the lattice) through a process called free-flight that executes linear interpolations on the grid (see figure 2). If a material is encountered, through a stochastic event selection, the code executes interaction routines that can modify both the state of the lattice and the trajectory of the particle (therefore even stopping it).

In general, when a MC code is launched, given a stochastic distribution, it executes routines (also with a random selection) that are functions that modify the states and must be repeatable to represent the physical processes. In this program, such routines are hard-coded in Fortran sources that decode the probability of an event depending on matrices called interaction matrices. The chemistry of reaction is read by reaction matrices too. In this way, the operator can edit these files and turn the physics on and off as appropriate.

Before starting the simulation, the dimensions of the box are the first parameters to be selected, then it is necessary to choose which are the initial cell states of this virtual material. The choice of possible states can be modified by the operator but the results of the reaction by-products with the plasma elements must be taken into account; moreover this choice must be consistent also with the interaction routines. After this, the initial material geometry and its dimension must be added.

We distinguish three types of tables: those of the species (see table 3), those of the reactions (see table 4), and the one of the events (table 5). The set of simulation processes constitutes the set of simulated physical phenomena that are entered via subroutines (divided in 'bulk' and 'surface'). While changing the chemical elements consists of updating the species' matrices through databases, adding a new process, in this

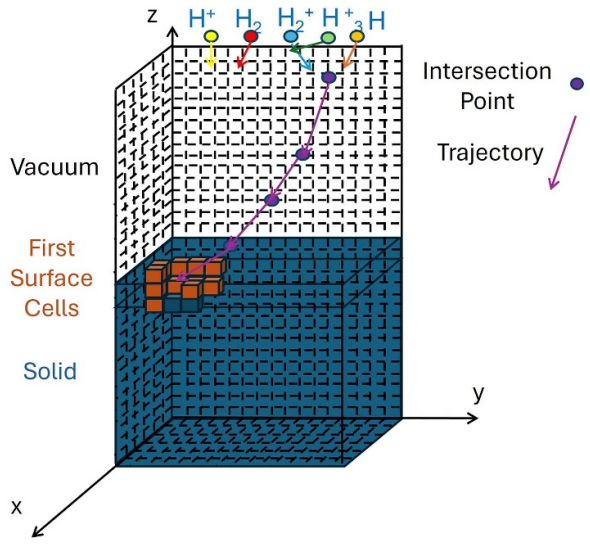

Figure 2. Free flight and penetration of a MC particle inside the material. The particle does not interact until the code identifies a cell in the lattice. On surface ones (indicated in orange) surface processes are activated, on volume ones (in blue), volume processes are activated.

Table 3. List of particles respectively defined in the MC code as ions, neutrals, and as by-products on the surface and in vacuum. Each of these is recognized in the code by an integer (index).

MC particles				
Index	Cell type	Neutrals	Ions	By-products
0	Vacuum			
1	W	H	H^+	W
2	WW	H_2	H^-	WW
3	WH		H_2^+	WH
4	WH_2		H_3^+	WH_2
5	WH_3			WH_3
6	WHW			WHW
7	WH_2W			WH_2W
8	WH_3W			WH_3W
9	WH_4W			WH_4W
10	WH_5W			WH_5W
11	WH_6W			WH_6W

version of the code, consists of editing subroutine files. The list of routines (with their respective names) activated for this paper is provided in table 5. The output of the plasma simulator is properly transformed to become the plasma particles injection. This means, as already mentioned, defining the objects to be tracked, but also their injection parameters in terms of energy (spectrum) and angle (distribution). The flux ratios, the temperature, and the potential are stochastically interpreted resulting in proper MC particles spectrum. In fact, it is possible to evaluate the dose for each specie i from the flux definition:

$$\Phi_i = \frac{N_i}{St_{\max}} \tag{17}$$

Table 4. Surface reactions between a plasma neutral particles and the surface adopted in the MC code. Each reaction changes the state of a cell. Starting from a certain Cell type and adding the atoms of the incoming MC particle it evolves toward a new Cell Type. Not allowed reactions are indicated by the symbol $*$.

Reaction table					
Index	Cell type	H		H_2	
1	W	WH	(3)	$WH2$	(4)
2	WW	WHW	(6)	$WH2W$	(7)
3	WH	$WH2$	(4)	$WH3$	(5)
4	$WH2$	$WH3$	(5)	$WH3(H)$	(5)
5	$WH3$	*	(5)	*	(5)
6	WHW	$WH2W$	(7)	$WH3W$	(8)
7	$WH2W$	$WH3W$	(8)	$WH4W$	(9)
8	$WH3W$	$WH4W$	(9)	$WH5W$	(10)
9	$WH4W$	$WH5W$	(10)	$WH6W$	(11)
10	$WH5W$	$WH6W$	(11)	$WH6W(H)$	(11)
11	$WH6W$	*	(11)	*	(11)

Here S is chosen to be equal to the box surface and $t_{\max}$ will be the total simulation time. Once the dose of a reference specie is fixed, the others must be in proportion with their relative fluxes. The MC particles are selected to preserve these proportions and when a MC particle is chosen, the counter of the dose increases, and the free flight starts activating the proper routines for that particle when the surface is reached.

In terms of the starting angular distribution, the plasma neutrals assume a cosine function, while charged particles are initialized according to the following shifted Maxwellian distribution:

$$\Gamma_{\text{ion}} = \frac{e^R}{\sqrt{\pi}}\left[\sqrt{R}\sec\theta\, e^{-R^2\sec^2\theta} + \frac{\sqrt{\pi}}{2} erfc\left(\sqrt{R}\sec\theta\right)\right]\cos\theta. \tag{18}$$

Here R is meant to be the energetic parameter: $R = eV_i/k_bT_e$. This version of the code is able to evaluate ion penetration (see [46] for the formalism of the binary collision approximation BCA method), etching, sticking and sputtering process. The same etch/deposition simulation framework of the baseline code (implemented in Fortran 90) provided by Campo *et al* [32] is assumed but current version is formulated in a 3D crystal lattice. In the same paper, the authors show that this distribution provided good agreement with the experimental data.

The choice of a shifted Maxwellian comes from the acceleration that the ions undergo due to sheath potential modifying the initial distribution (assumed as Maxwellian). This distribution is compatible with the theory underlying the calculation of the sheath potential [52]. As regards the distribution of neutrals, the Lambertian is chosen to guarantee an equi-probable distribution on the material starting from a flat surface (the boundary between plasma and simulation box). However, we noticed that other distributions for ions and neutrals can be provided by the users as input file in the code.

Table 5. Description of MC events, each involving an MC particle and an MC cell. Here I and N stand for ions and neutrals respectively. The graphic representation of an event in volume has been divided into 4 sub-panels which describe the positions assumed during the motion of an ion. The graphical representation of a surface sticking event has been divided into 2 sub-panels which include the motion and final position of an H_2 molecule.

MC events			
Event:	MC Flight	Volume (I)	Surface
Routine:	(1) FreeFlightN 3D (2) FreeFlightI3D.	Ionbulk3D	IonSurf3D and Surface (N);
Phenomena:	(1) Motion in void (N); (2) Motion in void (I).	(a) Etching (function); (b) Deposition (I) (table).	(a) Impingement (I) (matrix); (b) Sputtering or IEE (I) (function); (c) Sticking (N) (function).
Graphic representation:	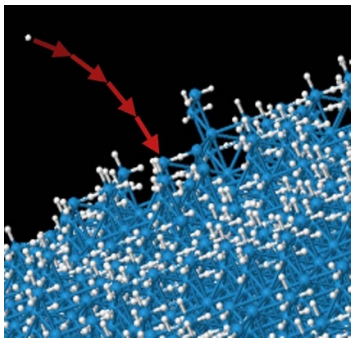	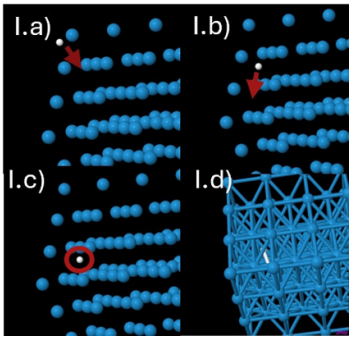	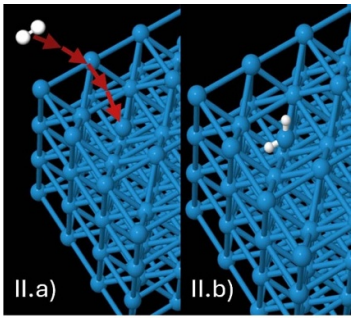

Moreover, our code has been upgraded in terms of management and flexibility of 'particle' and 'reaction' lists which were hard-coded in the previous version [32]. These particle lists include all the MC particles recognized and used by the code through a marker index, and they are normally divided as follows:

- 'cell type particles',
- 'neutrals',
- 'ions',
- 'by-product particles'.

A cell type particle is one of the different typology of occupation state of each MC lattice cell, assumed as body centered cubic (bcc) in this paper, according to a W wall composition. The total number of these states is $N_{\mathrm{in-cell}}$. Similarly, 'neutrals' and 'ions' particles are the typology of particles coming from the plasma and responsible for the erosion processes of the walls. The number of these states are respectively N_{neu} and N_{ions}. There are also N_{prod} 'by-product particles' that consist in the residuals of the interactions between incoming and facing particles. In surface reactions, the etching which emerge from the removal process (in form of gas particle) can be redeposited after a subsequent ballistic path in the void region (see [31]). For instance, in our simulations for surface reactions, the following indexed MC particles have been defined according with the table 3. The evolving etch/dept profile is defined as the boundary between these two states: 'Cell type $= 0$', 'Cell type $\neq 0$'. There are 12 possible state values for a cell in these simulations. The state 0 corresponds to empty crystal cell (i.e. a di-vacancy in the W lattice). This is because, in ideal conditions, the unit cell has (exactly) 2 W atoms before interacting with an MC particle (those that come from a flight or a penetration) and over time each cell will change state (and eventually become empty it the proper sequence of events occurs). Stochastic occurrences of events are implemented depending on the status of: the incoming particle, the crystal cell and the reaction product. For instance, the sticking reaction $W + H \rightarrow WH$ is modeled as following. Initial state (cell state: 1) + (neutral state: 1) $\rightarrow$ final state (cell state $=$ 3). After a possible removal of the WH complex (by-product of state 3) the corresponding by-product can be re-deposited promoting an empty cell (state 0) to the WH (state 3).

2.2.1. Surface MC phenomena. The surface reactions occur in the cells of the boundary leading essentially to a modification of the cell index (e.g. if a removal reaction took place, the cell index would become 0). They can be classified in three categories: neutral absorption, ion activated events (etching and sputtering) and by-products deposition (more detailed below).

The neutral absorption leads to the modification of the cell type by this generic reaction scheme:

$$\mathrm{Surface(old)} + \mathrm{Neutral(old)} => \mathrm{Surface(new)} + \mathrm{Neutral(new)}.$$

After the reaction, the eventual Neutral (new) particle can continue its travel again in the void region following a subsequent ballistic path or interact with the wall. Its reaction

matrices have dimension $N_{\text{cell}} \cdot N_{\text{neu}}$ and include also the associated stitching probability matrix (i.e. the matrix in which is considered the probability that the given reaction occurs after the encountering between the Neutral particle and the Surface cell). An extract of the reaction matrix for H and H_2 neutrals is reported in table 4. Neutrals, in fact, interact with the in-cell states (left column) forming a new 'molecular state' (whose list index is indicated in brackets). Symbols and respective indexes are reported, whilst the code uses only the index for the updates of the cells after the reaction. Not allowed reactions are also indicated. They are characterized by a null value of the stitching coefficient. It is also imposed instantaneous release of full coordinated surface species (WH3, WH3 (H), WH6W, WH6W(H)) but, alternatively, a very large removal yield can also be included in the calibration with the same effects. In case of different reaction schemes due to intermediate states, it is possible to implement them, modifying lists and matrices.

Ion activated events are detachment events activated by ions impinging on the surface which are classified into two typologies: Ion Enhanced Etching (IEE) and sputtering. These processes are implemented similarly in the code of Chiaramonte [31] here distinguished by different angular expressions for the yield function. For IEE the yield is:

$$\beta_{\text{IEE}(\text{ion}-\text{surf})} = C_{\text{IEE}(\text{ion}-\text{surf})}\left[\sqrt{E} - \sqrt{\left(E^{th}_{\text{IEE}}(\text{ion}-\text{surf})\right)}\right] f_{\text{IEE}}(\theta), \tag{19}$$

where $f_{\text{IEE}}(\theta)$ is a function of the incidence angle θ (with a maximum at $\theta = 0$ and a large plateau (till e.g. $\theta = \pi/4$) [31]. While for the sputtering (SP), the yield is:

$$\beta_{\text{SP}(\text{ion}-\text{surf})} = C_{\text{SP}(\text{ion}-\text{surf})}\left[\sqrt{E} - \sqrt{\left(E^{th}_{\text{SP}}(\text{ion}-\text{surf})\right)}\right] f_{\text{SP}}(\theta), \tag{20}$$

where $f_{\text{SP}}(\theta)$ is a function of the incidence angle θ with a maximum at large angles [31]. In the above expression, E is the ion energy whilst $C_{\text{IEE}}, E^{th}_{\text{IEE}}, C_{\text{SP}}, E^{th}_{\text{SP}}$ are calibration parameters which depend on the cell-type ion couple. Therefore, similarly to the neutral absorption, they can be stored and uploaded from the database in the matrix format described in the subsection 'Surface MC phenomena' 2.2.1.

By-products deposition. Particles removed from the solid part of the structure can travel ballistically in the void region until they encounter again the solid surface or until they are annihilated at the boundary between the simulation box and the plasma bulk. In the case of a surface encounter event, the particle can be deposited on the surface. The by-products deposition is therefore an event where a cell with index 0, that is a first neighbour of a cell with index $\neq 0$, assumes the index of the by-product itself. The deposition is ruled by deposition coefficients (i.e. the probabilities of a given deposition event).

2.3. Setting of the crystal lattice in the KMC simulation box and mapping of the pre-processed samples

The feature size region is mapped in the simulation box using profile shapes that have to be fixed before running the code. Alternately, it is possible to upload the Scanning Electron Microscopy (SEM) section of pre-processed samples as described in [31, 32].

In this paper the cubic lattice of the simulation box is commensurate to the tungsten one with the conventional cell of length $a = 0.3157$ nm in which two W atoms are present with a distance of 0.2734 nm per cell (reproducing stable α-W body-centered cubic crystal structure). In this lattice the initial state is mapped. In case of graphic representation of the sample, in the images, each species can be distinguished by a specific color, which is the already applied methodology to different cell states.

Bigger cells can be also used if the size of the etched structure is too large for the atomistic resolution. In this case, the average number of atoms, A_{cell}, should be calculated in order to normalize the yield functions as $\beta \rightarrow \beta/A_{\text{cell}}$. Moreover, in this case, the gas particles will not represent a single atom, ion, molecule or moiety (a group of atoms or portion of a molecule) but a MC particle that has to be sampled appropriately. The frequencies/probabilities associated to the sets of reactions of the bulk elements (for instance C and Si or in our case W) are completely different, resulting in different tables of events which need to be implemented per each kind of constituent element. In particular, with respect to the single elements of the wall, the new particles formed as combination of the wall elements reacting with the plasma ones, could be either more stable (and tend to hinder the IEE), or less stable (boosting the IEE). Finally, we note that, in principle, this KMC framework could be also improved in order to consider the real space atomic distribution in compound lattices in a procedure called Kinetic Lattice Monte Carlo approach. However, this approximate scheme should be sufficient to describe accurately the erosion process in the case of the specific interaction with the plasma.

3. Results and discussion

In this chapter we demonstrate the potential predictions achievable by sequentially coupling plasma and feature scale codes simulating the plasma-wall interaction that evolves under the quasi-sequential physical processes of etching, erosion, sticking and sputtering. The results are discussed assuming a realistic experimental setup in which the proper measurements of plasma characterization and materials modification are also accessible. We present the outcomes as a combination of both tools starting from the plasma simulations, which are used as input for the KMC code. Finally we notice that parameters' calibration is not definitive, however the general trends seem to be respected, in agreement with remarkable cases in the literature.

In case of molecular plasma stoichiometry (as in the case of hydrogen), the molecular reactions set increases the complexity of the system. Molecular states are known to influence the percentage of H_m [30]. To validate the developed APIs, which generate and solve 'on the fly' a plasma model from the user defined reactions' set, a direct comparison with the literature has been done also in the case of simpler systems: an argon (Ar) plasma was also simulated. In fact, being a noble gas (therefore not very interacting and complex) and being well known in the etching literature, the comparisons are immediate. Results relative to the Ar case are presented in the appendix.

3.1. Settings

Without lack of generality, we fix the geometry of the plasma chamber in the cylindrical shape symmetry (radius $R = 0.05$ m and length $L = 0.68$ m). Applications to different shape and dimensions are possible with minor modifications. In accordance with the literature, the geometry related calibration parameters were fixed as $\gamma_h = 0.23$ and $\gamma_Q = 1$ [30].

The initial temperature was set at 273.15 K, while that of the neutrals (which remains the same as the ions' temperature) was set at 473.15 K. In the future updates of the codes the temperatures could be evaluated dynamically if needed.

At the bottom of the plasma chamber a tungsten wall is considered. In this region we simulate the material modification due to the interaction with the plasma at atomic resolution. Therefore, we assume that the initial simulation box for the wall is made by a portion of the W crystal with $L_x \times L_y \times L_z = 180 \times 180 \times 400$ conventional W cubic lattice cells of length $a = 0.316$ nm. The $L_x \times L_y$ surface is in contact with the plasma and periodic boundary conditions along the x and y direction are also imposed to emulate the configuration of an infinite surface. The plasma state, due to its pre-sheath and sheath potential, accelerates the positively charged particles against the wall.

The simulations were then carried out implementing a possible Design of Experiments (DoE matrix, a matrix of experiments designed to test systematically the statistical weight of a sequence of input factors [53]) with two control variables: the pressure and the power. The power varies from 500 W to 1500 W with a uniform step of 250 W. The particles' flows constitute the real control variables as an incoming pressure which, however, is automatically modified by the code according to the evolution of the components percentage during the plasma discharge. For this reason, the results are discussed as a function of the outgoing pressures, which are those that regulate the flows, being also the initial condition for the KMC simulation. Five output pressure points are thus chosen to build the DoE matrix: 2.03 mTorr, 12.18 mTorr, 22.33 mTorr, 32.47 mTorr and 42.60 mTorr.

The simulated points are chosen to guarantee a link with the SOL region, according with the contemporary design of a nuclear reactor. The flows must be therefore compatible with the orders of magnitude although the apparatus is linear. With H gas, this occurs in ranges from unity to hundreds of mTorr in pressures and in ranges from hundreds to thousands of watts in power. In this way, temperatures of the order of eV and concentrations of approximately 10^{10} particles cm^{-3} are reached, obtaining fluxes of 10^{22} particles (m^2 s)$^{-1}$.

The link between the flows of elements in plasma and those in terms of MC particles is achieved through the calculation of the characteristic time, dose and sheath potential for each point of the DoE.

Indeed, flows in the plasma code are defined as the quantities of particles per unit time impacting on a surface. Thus, having fixed the surface, once a reference dose has been chosen, the time of the phenomenon is easily obtained as explained in section 2.2. It is obviously also possible to choose a time interval and obtain the number of particles that arrive on the surface within that given time. However, the clock of this code coincides with the injection of H^+ ions (the other injection events are automated in proportion to the particle flows) and consequently it was chosen to fix a sample of 10^4 particles (MC H ionic particles) which are injected to the wall for each MC simulations.

3.2. Plasma results

Here we show the plasma behavior with respect to pressure and power in terms of temperature and concentration (fixing the geometry chamber conditions of the chamber as stated before).

As shown in figures 3((*a*) and (*b*) panels), the electronic temperature manifests a monotonic decrease with pressure in the whole range of power here considered, while the density shows a non-monotonic dependence on power as evident from the lowest power case. This is due to the possibility at low power of activating further ionization processes rather than increasing the average energy of the electrons. In any case, over a certain pressure the temperature variations with the power tends to reduce, while the variation in electron density is still considerable.

Due to similar consideration, as shown in figures 3((*c*) and (*d*) panels), as the power increases the temperature decreases while the electrons' concentration increases.

The total sheath potential drop at the plasma wall interface is more influenced by temperature than by electron density. This statement is clearly demonstrated by the cross comparison between figure 3 and the sheath potential values derived as a function of the control parameters and shown in figure 4. In fact, the electron density does not change significantly with the pressure in this regime, while the density of lines in the potential solutions is very similar to the solutions that show the temperature trend.

It is possible to verify how the results for electron temperature and concentration are in line with those of other authors. In the paper of Samuell and Corr [26] two sets of experimental results are discussed. For a power ranging from 100 to 1200 W and a pressure of 10–100 mTorr (reactor GEC reference cell with a radius of 80 mm and a reactor length taken to be 50 mm) with the same order of 100 sccm (not relevant according to the author from 10 to 100 sccm) it is noticed that the orders of magnitude and the trends are in agreement (temperatures

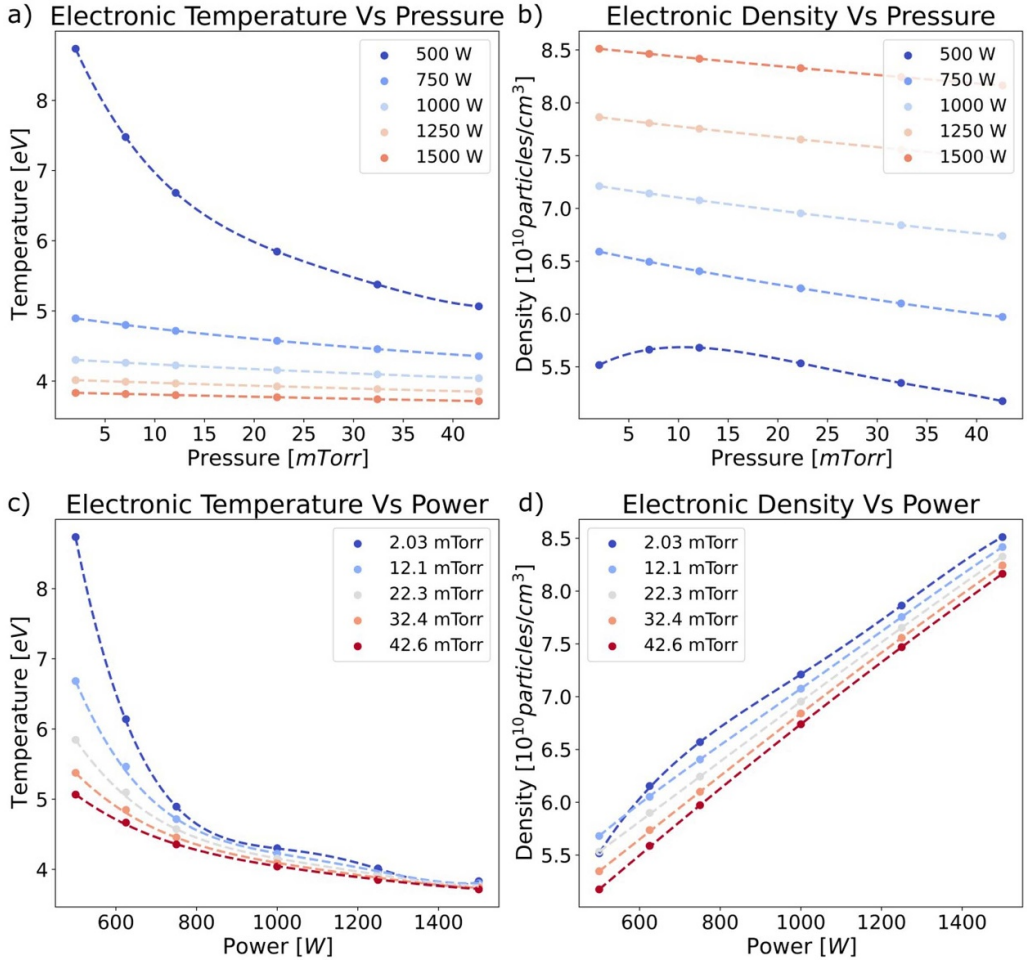

Figure 3. Electron temperature and density with respect to power and pressure for H stoichiometry in a cylindrical chamber of $R = 0.05$ m and length $L = 0.68$ m. The temperature of the electrons decreases monotonically as the pressure increases from 2 to 43 mTorr (panel (*a*)) regardless of the power absorbed while decreases not monotonically as power increases (panel (*c*)). The electron density decreases with power from 750 to 1500 Watt, but its trend shows a change (also in concavity) between 500 and 750 Watt (panel (*b*)). Panel (*d*) shows an increasing trend for electron density versus power.

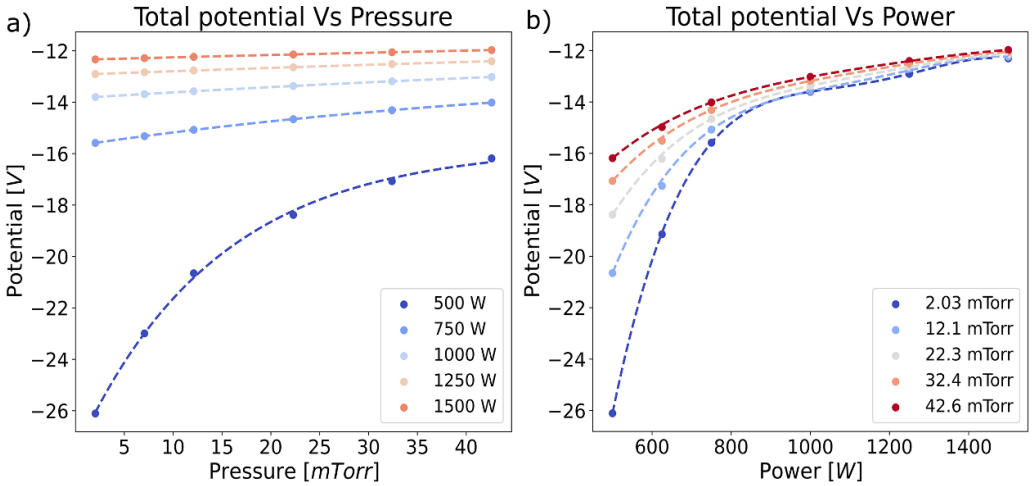

Figure 4. Total potential (meaning the sum of sheath and pre-sheath) with respect to power (panel (*a*)) and pressure (panel (*b*)) for a gas of H. Radius $R = 0.05$ m and and length $L = 0.68$ m. The total potential tends to increase with both power and pressure.

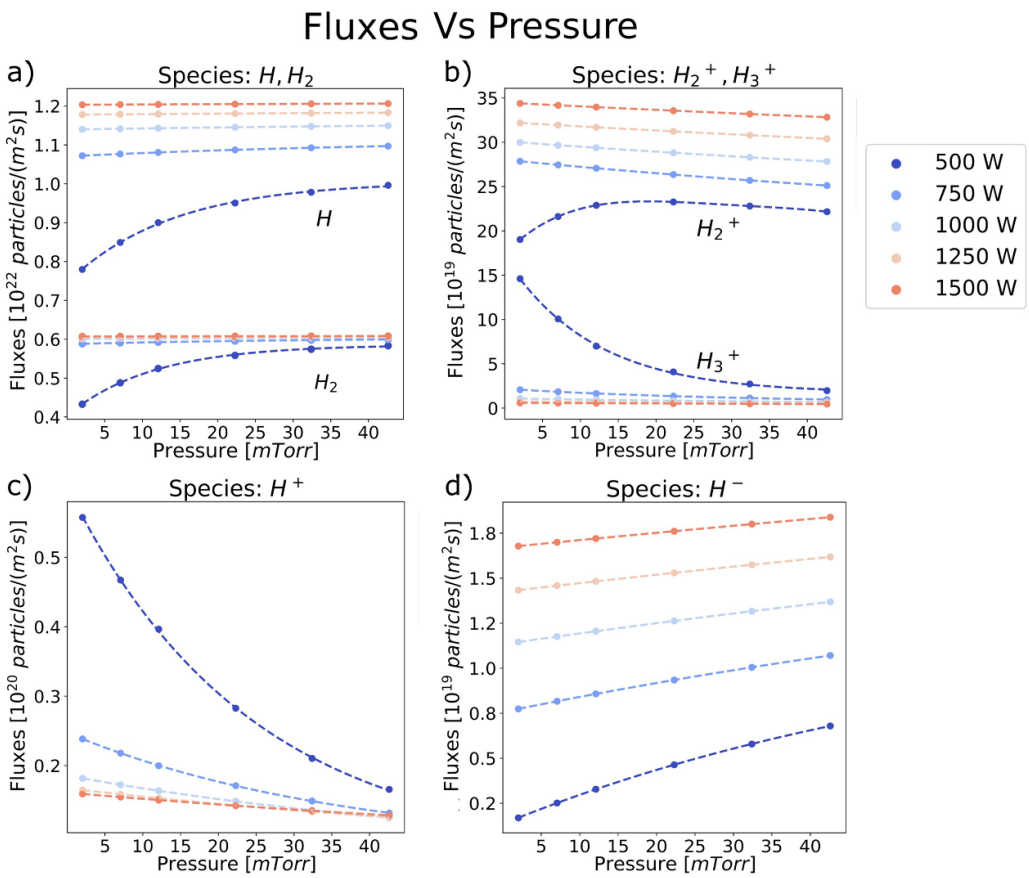

Figure 5. Components of the flows generated by the plasma simulator as pressure vary per each power (linear plasma device, radius $R = 0.05$ m and length $L = 0.68$ m). In panel a the species H and H_2 are shown. These grow with pressure and are the most abundant. The behavior of $H_2{}^+$ and $H_3{}^+$ ions is shown in panel (*b*). While $H_3{}^+$ decreases in general, the $H_2{}^+$ plot increase for small pressures (corresponding to a strong decrease in $H_3{}^+$). H^+ decreases monotonically (panel (*c*)) while H^-, which is the less concentrated ion, increases (panel (*d*)).

between 2 and 6 eV and concentrations between 10^9 and 10^{11} particles cm^{-3}). For the MAGPIE experiment (50 sccm) from 3 to 10 mTorr in a measurement between 200 and 1500 Watt (very similar to our conditions), an even better agreement is observed. Considering some experimental fluctuations, which however converge at a power of 1500 W (10 mTorr pressure) at 4 eV, the result of the simulations is still in agreement. A similar trend is also observed when the powers vary. At low powers and pressures of 12 mTorr our code overestimates the concentration by a few units, settling at 5.5×10^{10} particles cm^{-3} (500 W) compared to approximately 5×10^{10} for Samuell. The rest of the concentration results are in agreement. It is possible to carry out a similar analysis (although the chamber is a little different) also with Hjartarson *et al* [30] in the case of simulations with 100% hydrogen in their model.

In figure 5, we reported the values of fluxes per each species changing with power and pressure. As stated before, the plasma fluxes are the quantities of particles (of a certain species) coming from plasma that meet the surface in the unit of time, given the initial conditions. This data is the main information that is needed to drive the KMC simulations and quantify the time step, together with the sheath potential value.

To calculate the fluxes, each concentration must be multiplied for the right speed term. In case of ionized particles, it is possible to use the Bohm velocity (and this is the option we have chosen for convenience), but in the case of neutral, the diffusion coefficient must be used.

3.3. *Kinetic Monte Carlo results*

Detailed results of the erosion processes are shown in this subsection, with respect to time, for the DoE point of reference 22.33 mTorr and power 1000 W. This choice was made for purely demonstrative purposes as the procedure is repeated for all points provided by the plasma code and then simulated by the KMC. These results thus represent the predictions which can be extracted for each given point of simulated matrix.

In this DoE point we provide time dependent information about the total erosion (the erosion rate can be derived through the KMC time) and roughness. The procedure adopted is therefore an example of how to extract the physical information before the formal sequential coupling of the two codes. In fact, although the KMC is not definitively validated by experiments, it is able to provide results about the first surface composition.

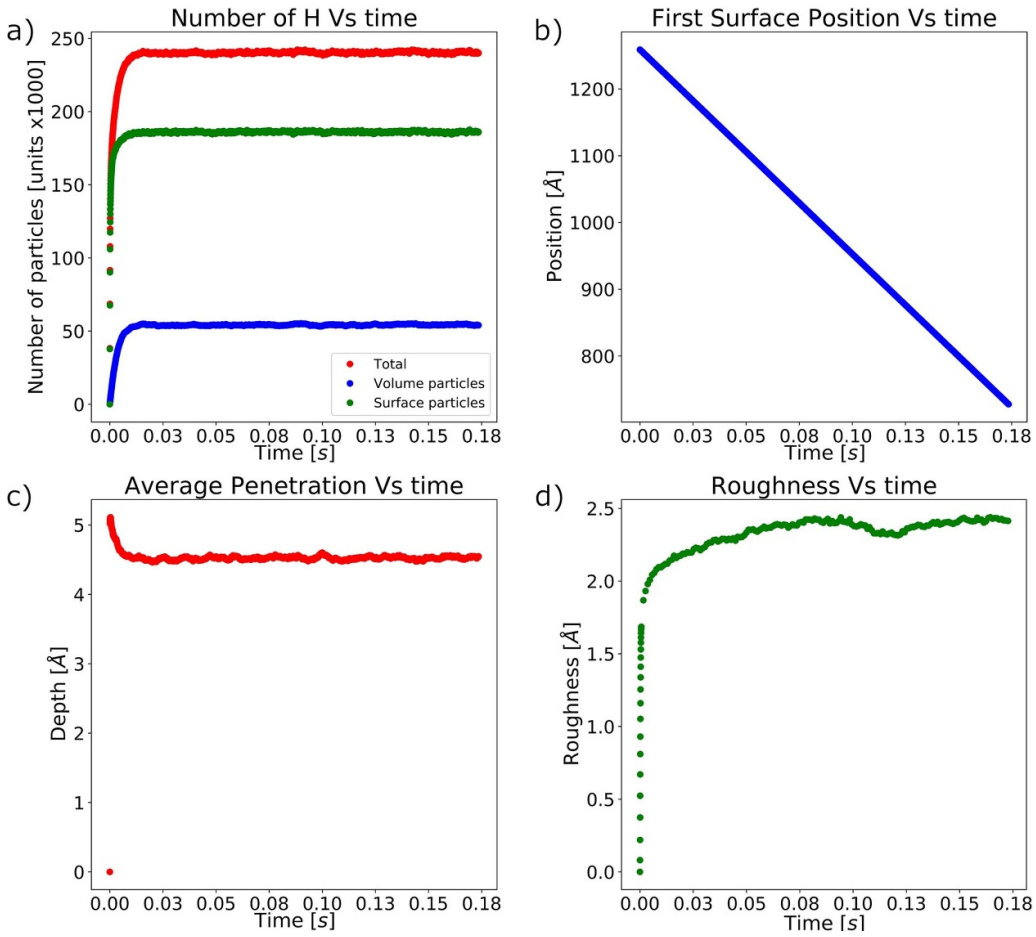

Figure 6. Sequentially coupled simulation of plasma emitted by cylindrical linear plasma device (Radius $R = 0.05$ m and length $L = 0.68$ m) on wall ($180 \times 180 \times 400$ lattice sites of W bcc). Injection power 1000 W, thrust 22.33 mTorr, dose 10 000 H^+ particles. Panel (*a*) shows the total number of hydrogens that have attached to the surface or penetrated the wall over time with an insertion flux of around 3×10^{21} particles $(m^2\ s)^{-1}$ for low coverage conditions. Panel (*b*) shows how the wall is abraded by the plasma by graphing the position of the first surface over time. Panel (*c*) shows the average penetration of all H particles within the solid. Panel (*d*): roughness of the wall with respect to time.

In these plasma-provided initial conditions (in which the total potential in absolute value is low with respect to an average etching condition), the erosion is limited and no particular artifacts are distinguished as a consequence of the irradiation.

As we can see in figure 6(*b*), the first average surface position decreases constantly. Scanning from the top of the box, the first surface is simply identified as the locus of molecules (cells with state different from zero) that have other particles below and no one above.

The nominal position of this surface follows a step evolution. In fact, it is defined as the closest integer to the mean surface. The average, time by time, of the heights of the elements of the first surface, provides the average First Surface Position, which is no more an integer number. However, for long enough simulations, the results become the same and both descend linearly.

To take into account the fraction of H deposited on the surface, and the one deposited inside the material, we arranged figure 6(*a*). It shows the number of particles, with respect to time, growing either inside the material or on the surface. Sometimes it can happen that groups of chemisorbed H atoms or H-W complexes, released as a result of the erosion, are re-adsorbed at the surface. At the moment, the code underestimates their recycling dynamics (i.e. for particles which go out of the mother simulation box), but the plan is to implement it in future developments. This process can lead to fluctuations in the total number of particles, which however remains limited. It is possible that, at least locally, these particles could influence the plasma state interacting with the fuel atoms to form H and W compounds that can be redeposited [14].

In the same figure 6, the average penetration graph of particles inside the material is presented (panel (*c*)). It reaches a peak and then decreases to become stationary. The reason is that, increasing the number of incoming particles, the material recedes due to the erosion, and therefore such particles, which penetrated into the bulk at an early stage, always seem to approach the first surface changing the averaging result over time. In any case, increasing the statistic, an average penetration is quickly reached. It will vary positively or negatively in a random way with the root of N. Obviously it is possible

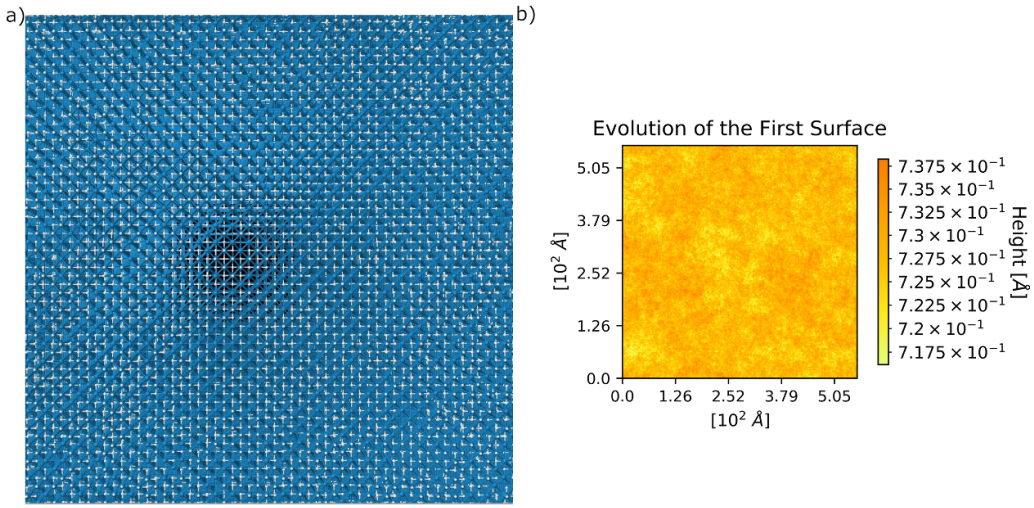

Figure 7. Top view (*xy* plane) of the atomic lattice (panel (*a*)) and the equivalent AFM image (*b*) of W PFM exposed to hydrogen plasma for the combined simulation in the central point of DoE matrix (1000 Watt, 22.33 mTorr), as generated by a linear accelerator ($R = 0.05$ m and $L = 0.68$ m), at a dose of 10 000 H^+ particles. In the lattice view H is white while W is blue. The AFM image (180 × 180 lattice sites) shows the deepest craters in yellow while the highest peaks in orange as shown by the colorbar on the right of the graph.

to discriminate the particles penetrated at any given time to make an accurate measurement of penetration. However, this raw distribution is more similar to the experimental measurement conditions.

3.4. Molecular distribution of the first surface

An example of the structural details, relating to material transformations due to plasma interactions is provided below.

It is possible to define the map of the elements which constitute the first wall surface, together with their relative positions. It is read as a matrix by the MC code. Figure 7 is the cross section image of the tungsten plate for the simulation with the same conditions of figure 6(case of pressure 22.33 mTorr and power 1000 W). The equivalent of an Atomic Force Microscopy (AFM) image (figure 7(*b*)) is realized to compare with the lattice in the same plasma configuration (figure 7(*a*)). In fact, figure 7(*a*) is the image of a cutaway, close to the first surface, made in xyz format. Inside the material (near the first wall), it is in fact possible to reconstruct the state of each cell by presenting an image with a sensitivity of the order of the angstrom. From our first surface matrix, the topology of the surface with the same sensitivity of few angstroms is reconstructed. It is also possible to repeat this operation step by step over time and combining such matrices to form a gif file which represents the time evolution of the system. To obtain these pictures, combined etching, erosion and sticking routines were activated in the code.

3.5. Combined results

We performed 25 simulations spanning the space of initial conditions in terms of powers and pressures as stated before. In this specific framework, concerning fast simulations, there is no plasma contamination, therefore, the simulations are carried out with a sequential coupling. For each couple of initial conditions (pressure and power), there is a flux solution. Such a solution is a group of fluxes, representing the number of incoming particles on the unitary area respect to time for each species as already showed in subsection 'plasma results' 3.2.

The fluxes plotted in figure 5 may change with the boundary conditions of the chamber. The set of solutions represented in figure 5 and extracted from the DoE points, together with the total potential, constitutes the space of initial conditions for the KMC evaluator.

Taking into account firstly that changes in fluxes are not trivial and, secondly, that the results must be combined with the potential, it can be deduced that the coupling between the plasma and the wall (which represents the boundary of the plasma as a differential system) is a complex environment. This implies that the variation of a parameter does not trivially reverberate in the modification of another quantity. For this reason, by simulating the erosion for each point in the pressure-power space, a surface (in MC solutions) is constructed. In general this procedure does not build a one to one function.

The results of the combined approach can be seen in figure 8; these can be plotted (expressed with the same dose) in terms of erosion, penetration length and roughness. The more energetic conditions correspond to a greater retreat of the first surface and a greater penetration length. As first instance, the roughness formation depends on the activated processes and not on the energy associated with them, therefore, even if the roughness evolution depends on the dynamic conditions of each single process, in this energetic range, it remains limited because we are neglecting the collective motions of the gas.

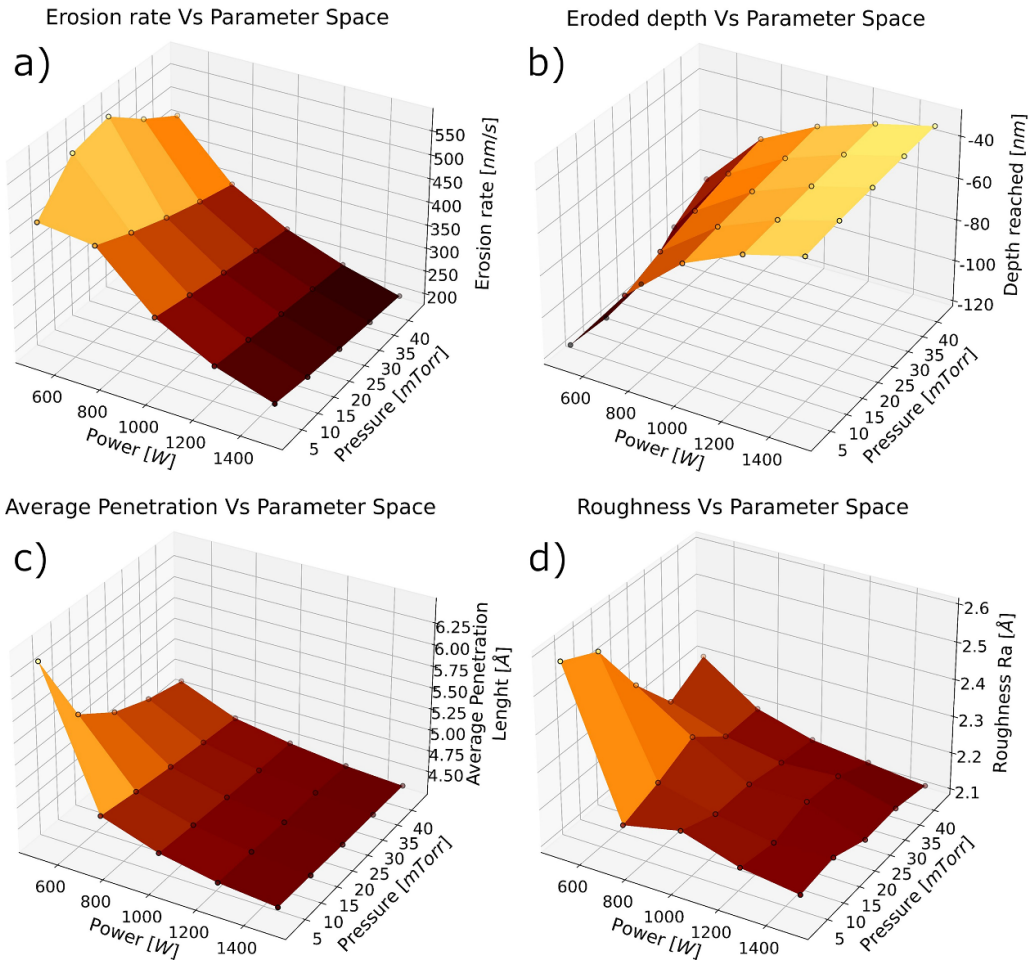

Figure 8. Results of sequentially coupled simulations (linear plasma device and W wall are the same of figure 6 but the inlet parameters vary on the whole DoE matrix). In this image the color is indicative of the values reported on the vertical axis (i.e. the z-axis represents the color-bar). By varying the plasma injection parameters (power and thrust), the outputs of the MC are graphed: erosion rate in panel (a), Eroded depth in panel (b), Average penetration in panel (c) and Roughness in panel (d). The trends of these variables are almost monotonic. Erosion is greatest where ion penetration is greatest.

3.6. Overall behavior of the system

As a reasonable trend, the increase of ion fluxes, in terms of both dose and energy, results in a faster erosion. Anyway, the real contribution to the changes of the first surface position and morphology is due to the combination of different causes. In fact, although in the context of etching experiments this sheath potential is considered low, the coupled action of the H_2 molecules, which act chemically on the surface, plays a fundamental role on the PFM evolution. When the power increases, atoms tend to ionize and consequently to increase the electronegativity of the system (precisely the electron concentration).

At this energetic regime, some of the plasma energy is subtracted by the ionization process of H^- (phenomenon which appears enhanced if expressed in terms of pre-accelerated flux), resulting in a decrease in electronic temperature which consequently implies a global rearrangement of the concentrations, due to the temperature-dependent rates. The rearrangement is not linear by definition and this growth of concentration reduces effectively the energy per electron.

In principle it should bring the system to balance through volume reactions, increasing the positive ions concentration. However, the plasma is coupled with the container which also influences the balancing.

The strong decrease of the electron temperature, and the increase of the $H_3{}^+$ concentration (that influence the overall electronegativity), therefore result in a reduction of the sheath and presheath potential (in absolute value). From an effective point of view, the neutral fluxes seem to grow together with those of $H_3{}^+$ but the sheath potential in the meantime decreases leaving the plasma-wall interaction dependent only on the neutrals.

This process has a positive implication on the durability of the materials because, with a larger dose and being the temperature lower, it is possible to transmit a lower energy per particle, that implies a lower etching and average penetration length while the percentage of energy transmitted to the external environment increases.

However, in case of lower penetration lengths, the concentration of the H immediately under the first surface would be larger, resulting in an increased interaction between the interstitials. In fact, the dynamics of the H bulk diffusion leading to the formation of hydrogen bubbles is not taken into account in these simulations and could improve secondary processes as with a closely related loss of material performance on long-term activities. For instance, for He gasses, the dynamics of the bubbles is fundamental in fuzz formation for fluences and energies of the same order in tungsten and molybdenum ($\Phi \approx 10^{25}$ at m^{-2}, E ≈ 30 eV) [54].

A similar argument can be repeated for pressure variations. However, an increase in pressure does not result in a significant change in either the penetration length or the total erosion (at fixed dose).

The dynamics is therefore mainly driven by the potential: the increase in fluxes is indeed marginal because the Bohm velocity depends on the electromagnetic thrust while the fall in potential is equally recorded. This is reasonable because the electronic density does not increase with pressure (as opposed to what is recorded when the power increases) and it happens because the energy must be shared with multiple molecules.

Therefore, in general, although it is true that a greater boost pressure leads to a higher flux which produces more erosion; in the case of a comparison with a fixed dose, the overall effect of the pressure, as a first approximation, results only in a loss of potential. This explains the asymmetry in the behavior of the graphs in figure 8 under pressure and power variation.

Regarding the known phenomenology, there is a large literature on the damage generated by H (and also by He) on W or tungsten compounds. These are divided trying to cover different energies, temperatures and fluences or, in any case, tend to measure different quantities mostly based on the imaging realized by electron microscopy.

A 2020 paper [55] explains how damage by hydrogen generates blistering at the mesoscale due to microscopic damage. In fact, in terms of damage, blistering for H is the analogue of fuzzing for He although the phenomena are different. Furthermore, H and He can interact with each other in aging processes. In our simulations it is possible to observe an accumulation of hydrogen that penetrates beyond the coverage layer. This is because H atoms combine with each other forming hydrogen gas (H2) due to their high reactivity.

Another recent experiment on a linear device [56] with fluxes comparable to those generated in our simulations (actually for deuterium on alloy W-V) revealed blistering caused by H and in particular High-resolution Transmission Electron Microscopy (HR-TEM) images show severe distortion in W thin area, indicating local stress and disordered structure formation on the W surface of the same order that is observed in our simulations.

4. Summary and conclusion

A sequential multiscale simulation code was designed and set up to describe the evolution of PFMs in a nuclear fusion environment. Although the code is still under development, it was optimized and tested in case of linear geometry (i.e. to reproduce the physics of linear plasma devices).

Such a simulator consists of a sequential coupling between a 3D-KMC code, that evaluates the atomic dynamics of the first wall, and a plasma simulator which evaluates the physical quantities (electronic temperature and concentrations, fluxes and sheath potentials) necessary to characterize the plasma and launch the KMC.

The coupling of these codes depends both on shared information about the physical quantities affecting the plasma state and on the definition of the MC particles that are created in plasma. The combination of these two codes has been implemented in practice and it is able to simulate the evolution of the PFM reaching the sensitivity of the tungsten unit cell.

The plasma model extends in the context of the fusion research methods already adopted in the recent scientific literature and developed in electronic device manufacturing etching contexts. Here it has been adapted to simulate the typical parameter space of the devices currently performing fusion plasma experiments with the aim of producing and measuring the erosion of PFMs.

Our model is able to simulate homo and ambipolar plasmas taking into consideration the excited molecular states and different types of ions. The surface reactions are part of the model and, through geometrical chamber parameters, it is possible to extend the physics reproducing a 3D model [20, 49]. Our approach is indeed to insert the reaction parameters into specific databases in order to make the code adaptive and to weigh the contribution of the various physical phenomena.

We calibrated the code on both H and Ar, with the intention of replicating the literature results in the working ranges of common plasma chambers and at typical working pressures (for H between 2 mTorr and 42 mTorr) and powers (between 500 W and 1500 W). According to the previous literature, the plasma temperature for the Hydrogen composition is constrained between 4 eV and 10 eV with relative electron densities around $5–8.5 \times 10^{10}$ particles cm^{-3} [27, 28, 30]. In fact, starting from geometrical conditions, power, flow pressure, and input gas stoichiometry, it is possible to obtain: molecular concentrations, flows, electron density, electron temperature, sheath potential and pre-sheath potential.

Once the sheath potentials have been evaluated and the fluxes extracted, the code is coupled to the KMC model which simulates etching, sticking, sputtering and penetration phenomena. Each point in the injection parameter space has been analyzed showing an erosion rate spacing between 200 and 550 nm s^{-1}. A global study was subsequently carried out at the same dose of H^+ as shown in figure 8. As a result of the global analysis, if the power increases and the other parameters are fixed, the erosion rate decreases while the roughness remains almost constant. Changes in thrust do not modify the erosion trivially since the main parameter affecting the erosion rate is the total flux.

Slightly different is the behavior of the penetration length. It is because the acceleration potential, i.e. the main parameter affecting the penetration, is linked to the DoE space (meaning

to the plasma pressure and power with fixed chamber) according to equation (16), and therefore through the electronegativity which lowers while the pressure increases.

To facilitate the visualization of the results, the code provides us with 3D images of both the global analyses as a function of the parameter space, and the maps of the PFM first surface for each time slide. These maps allow observing the nanoscopic dynamics of the material. AFM-like images have been mounted in gif files to provide the time evolution of the first surface for each point. Those files can be employed in case of comparison with both the experiments or other configurations which lead to a different dynamics (see for instance variations of the angular distributions).

The possibility of updating the list of physical interactions allows us understanding which ones are the most relevant (at least at the calibrated energy regimes), however the physical processes simulated so far do not provide a noteworthy result on the increase in roughness. The Ra roughness has given results around 0.22 nm for a pure H_2 gas at pressure 22.33 mTorr and power 1000 W. This could result from either a calibration which is not yet complete or an initial condition set as perfect crystal. The result, however, underlines that to describe the evolution of surface roughness, there is a need to include other competing physical phenomena. In general, the order of magnitude of the analyzed physical quantities appears realistic.

The description of global motions of the gas, responsible for blistering or fuzzing (for He) and depending on bubble formation and dynamics, is still under research. The temperature of the material certainly plays a role in this process but studying the interactions between the elements penetrated by the surface (whose dynamics are not trivial) is also important.

This requires a dedicated study to be included as a new process in the MC; however, the code is designed to be updated inserting new routines in future. Their inclusion will lead to changes in the current morphology: in fact, a different evolution is expected due to new interactions between the bulk and the first surface.

A possible extension of the KMC could foresee dedicated routines for the motion of the gaps. It could be coupled to a continuum algorithm for the description of the bubbles evolution (and in general of physical processes on larger temporal and spatial scales).

A similar statement also applies to materials: the results have been provided for tungsten impinged by hydrogen components but the code may consider other elements and, by changing nanoscopic dynamics, mesoscale processes could appear different.

Furthermore, nowadays, very complex studies on the W damaging have been carried out highlighting how the motion of the gases is important for the result. A very comprehensive paper in the field of is provided by Li *et al* [57]. Rescaling on surface and fluence, we obtain retention values very similar to the ones obtained by Zhao *et al* [58] (4.7×10^5 compared to 1.0×10^6). However, this result must be evaluated as an order of magnitude because some routines have not been implemented yet in our code. In the same review (Li *et al* [57]), mention is made of studies which, for modeling purposes, include the evaluation of roughness, but under different energy regimes. Furthermore, much literature includes studies of H and He as a source of coupled damage and this review underlines the following concept: 'it is still difficult to give an exact relationship between H/He retention behaviors in W and surface damage/-microstructures, and even with many controversies.' In fact, the mesoscale study of gaseous processes related to H and He could provide important results for concrete developments of the subject. As a future evolution, it could therefore be useful to try to include both elements in the model.

Acknowledgments

This work was supported by the Joint Research Agreement (JRA) between ENI and CNR 24 Marzo 2019. The sources of the codes will be released to interested scientists upon reasonable request.

Conflict of interest

The authors declare that they have no known competing financial interests or personal relationships that could have appeared to influence the work reported in this paper.

Appendix

A.1. Details of theory

As already mentioned, it is possible to obtain solutions of the system (8)–(12) for the unknown $T_e(u_b)$, α, α_0, n, l, x_0, imposing both the following expressions [28]:

$$h_c = 1/\left(\gamma^{1/2} + \gamma_+^{1/2}\left[n^{*1/2} n_+/n_- 3/2\right]\right), \tag{21}$$

$$n^*[v] = (15/56)\frac{\eta^2 v_{i_{th}}[v]}{k_{\rm rec}\lambda_i[v]}. \tag{22}$$

Here $k_{\rm rec} \approx 5x10^{-14}{\rm m}^3{\rm s}^{-1}$ is the rate coefficient for mutual neutralization in the bulk plasma, while $\lambda[v]$ is the mean free path for each species $[v]$ and is given by $\lambda_i = \sum n_j \sigma_{ij}$, where σ_{ij} are evaluated rising by squared and multiplying for π the effective radii matrix terms (given in table 6). Furthermore η is equal to $2T_+/(T_+ + T_-)$, and v_{th}^i is the ions thermal speed. According with the paper of Lee and Lieberman [43], based on the work by Lichtnberg *et al* [48], the sheath edge density is obtained in the following form, from which they derive h_{l0}:

$$n_s = n_{e0}\frac{1+\frac{2\alpha_0}{\gamma}}{1+\alpha_0}\left(\frac{1}{1+(l_p u_B/(2\gamma D))}\right), \tag{23}$$

where $\gamma = T_e/T_i$. Moreover, h_l can be taken in a more general form in the case of transitions from low to high pressures and both for electropositive to electronegative regimes [43]:

$$h_{l0} = \frac{1+3\alpha_0/\gamma}{1+\alpha_0}\frac{0.86}{\left[3+(L/2\lambda)+(0.86 L u_B/\pi D_a)^2\right]^{1/2}}. \tag{24}$$

Table 6. Effective radii used for the calculation of the cross sections in the equation (29) in the case of the interaction between the species in the column with the one in the row.

Effective radii for scattering cross section $[10^{-10}]$ m						
Species	H	H^+	H^-	H_2	H_2^+	H_3^+
H	1.35	1.35	1.35	1.52	1.52	1.68
H^+	1.35	1.35	1.35	1.52	1.52	1.68
H^-	1.35	1.35	1.35	1.52	1.52	1.68
H_2	1.52	1.52	1.52	1.68	1.68	1.83
H_2^+	1.52	1.52	1.52	1.68	1.68	1.83
H_3^+	1.68	1.68	1.68	1.83	1.83	1.995

Table 7. List of Argon plasma reactions with respective index, coefficients and thresholds. The notation is analogous to that of table 1.

Argon reaction in plasma			
Name	Reaction	Coefficients ($cm^3\ s^{-1}$)	Threshold (eV)
R101	$Ar + e^- \rightarrow Ar^+ + e^- + e^-$	$1.235 \times 10^{-1} \times e^{-18.69/Te}$	15.8
R102	$Ar + e^- \rightarrow Ar^* + e^-$	$3.71 \times 10^{-2} \times e^{-15.06/Te}$	12.0
R103	$Ar^* + e^- \rightarrow Ar^+ + e^- + e^-$	$2.05 \times 10^{-1} \times e^{-4.95/Te}$	3.80
R104	$Ar^* + e^- \rightarrow Ar + e^-$	2.0×10^{-1}	0.00
R105	$Ar^* + Ar^* \rightarrow Ar + Ar^+ + e^-$	6.2×10^{-4}	0.00
R106	$Ar + e^- \rightarrow Ar + e^-$	$-3.3 \times 10^{-4} \times \ln(Te) + 0.05$	$3. \times 5.486 \times 10^{-4} \times Te/39.948$
R107	$Ar^* \rightarrow Ar + hv$	3.0×10^{-4}	0.00
Name	Reaction	Coefficients (1/s)	Threshold (eV)
R108	$Ar^+ + \text{wall} \rightarrow Ar$	$3.0 \times u_{BHAr} \times (L/L_h + R/R_h)$	$7.00 \times Te$
R109	$Ar^* + \text{wall} \rightarrow Ar$	$Da[Ar^*]/(\Lambda^2)$	0.00

Here λ is the mean free path of the ions. The corresponding h_R can be written as:

$$h_{R0} = \frac{1+3\alpha_{\text{avg}}/\gamma}{1+\alpha_{\text{avg}}} \frac{0.8}{\left[4+(R/\lambda)+(0.8Ru_B/2.405J_1(2.405)D_a)^2\right]^{1/2}}. \quad (25)$$

D_a, for each species s, results as following [30]:

$$D_a[s] = Di[s](1+\gamma+\gamma\alpha)/(1+\gamma\alpha), \quad (26)$$

where

$$Di[s] = \left[1/D_K + 1/D_{\text{self}}\right]^{-1}. \quad (27)$$

In the absence of a magnetic field, the diffusion is determined by D_K and D_{self}, which are respectively the Kundsen diffusion term,

$$D_K[s] = (2/3)\, v_{th}[s]\, R, \quad (28)$$

and the Enskog self-diffusion term provided by Chapman's theory [59],

$$D_{\text{self}}[s] = \left[(8/3)\, diam[s,s]^2\, g_2[s]\, n[s] \left(\frac{\pi m[s]}{k_b T_n}\right)^{1/2}\right]^{-1}, \quad (29)$$

where $g_2 = (1-\iota/2)/(1-\iota)^3$, $\iota[s] = (\pi/6) diam[s,s]^3 n[s]$, and T_n is the temperature of the neutrals. *diam* represents the effective diameter for the collision of two generic species inside the reactions.

A.2. Test for other compositions

Before running the code for H stoichiometry, the plasma code was tested for the Ar one. Argon is a very common element in the etching simulation literature. The list of Ar reactions is presented in table 7.

The code has been evaluated entering an input stoichiometry of the pure element. As it is shown in figure 9(*a*), at a power of 50 W, for a chamber with a radius of 7.5 cm and a length of 10 cm, the experimental values of temperature varies between 3.5 and 2.5 eV for pressures between 5 and 70 mTorr [60]. Figure 9(*b*) shows how in a chamber of L = 8.5 cm, R = 5 cm, with a power of 100 W, the temperature is bounded from 4.2 to 3.5 eV while the pressure varies from 3 to 15 mTorr [61]. For a power of 600 W, in a chamber of 7.62 cm length and 15.24 cm radius, in a pressure range from 2 to 30 mTorr, the temperature decreases from around 5.5 eV to less than 3.5 eV (however the last one is an extrapolated point, identified with the empty dot).

In all these cases, our model describes the experimental results with a CL limit of the 90 %.

Moreover, in these conditions, while the electron concentration rises, the temperature decreases. This behavior is well

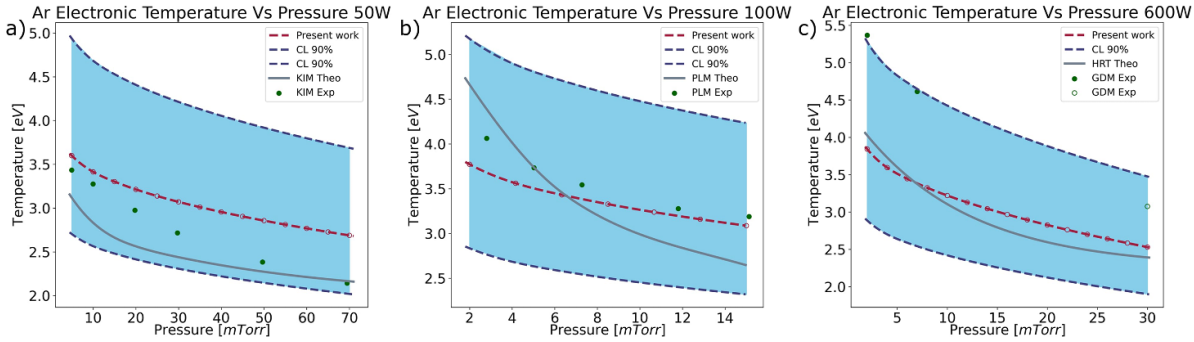

Figure 9. Electron temperature with respect to pressure for pure Ar stoichiometry compared to the literature. The results of this model are plotted in dashed amaranth (each simulation is indicated with empty dots). Two dashed blue lines are plotted to represent 90% of C.L. on the geometric parameters. The solid lines represent the theoretical models, while the experimental measurements are indicated with solid dots. Case (*a*): $L = 10$ cm, $R = 7.5$ cm [60]. Case (*b*): $L = 8.5$ cm, $R = 5$ cm [61]. Case (*c*): $L = 7.62$ cm, $R = 15.24$ cm, results for case of 100% Ar [30]. In all cases the trend is decreasing.

known, and is due to the definition of energy density, which increases with the product of concentration and temperature. In the same range of pressures, the electron concentration remains of the order of 10^{16}–10^{18} particles m^{-3} according to the same trend provided by the previous authors.

A.3. Specifications on sequential coupling of codes

This section describes the technical aspects that concern the passage of information between the plasma code and the MC simulator. A diagram is also provided: see figure 10.

The global input data are: Chamber dimensions (L,R), Power, Pressure, gas and chamber temperature, W Plate dimensions (height, thickness and depth). This data is used by all the codes of the program.

The input data that intervene only on the plasma are the Diffusion Info to which are added: Database of species, Database of reactions, Scattering parameters and radii; while the ones that only intervene on the material are: Routine selection and Calibration matrices (for Specie and Reaction).

The outputs of the plasma code are divided between the results for each single point of the DoE (Element concentrations, Electronic temperature, Electronic concentration) and those that are used for coupling with the KMC, which pass through a global code (the one that also provides the first plasma graphs). Once the KMC code has finished its run, the global algorithm performs data analysis, prepares graphs and images taking into account the results of both codes across the entire DoE matrix

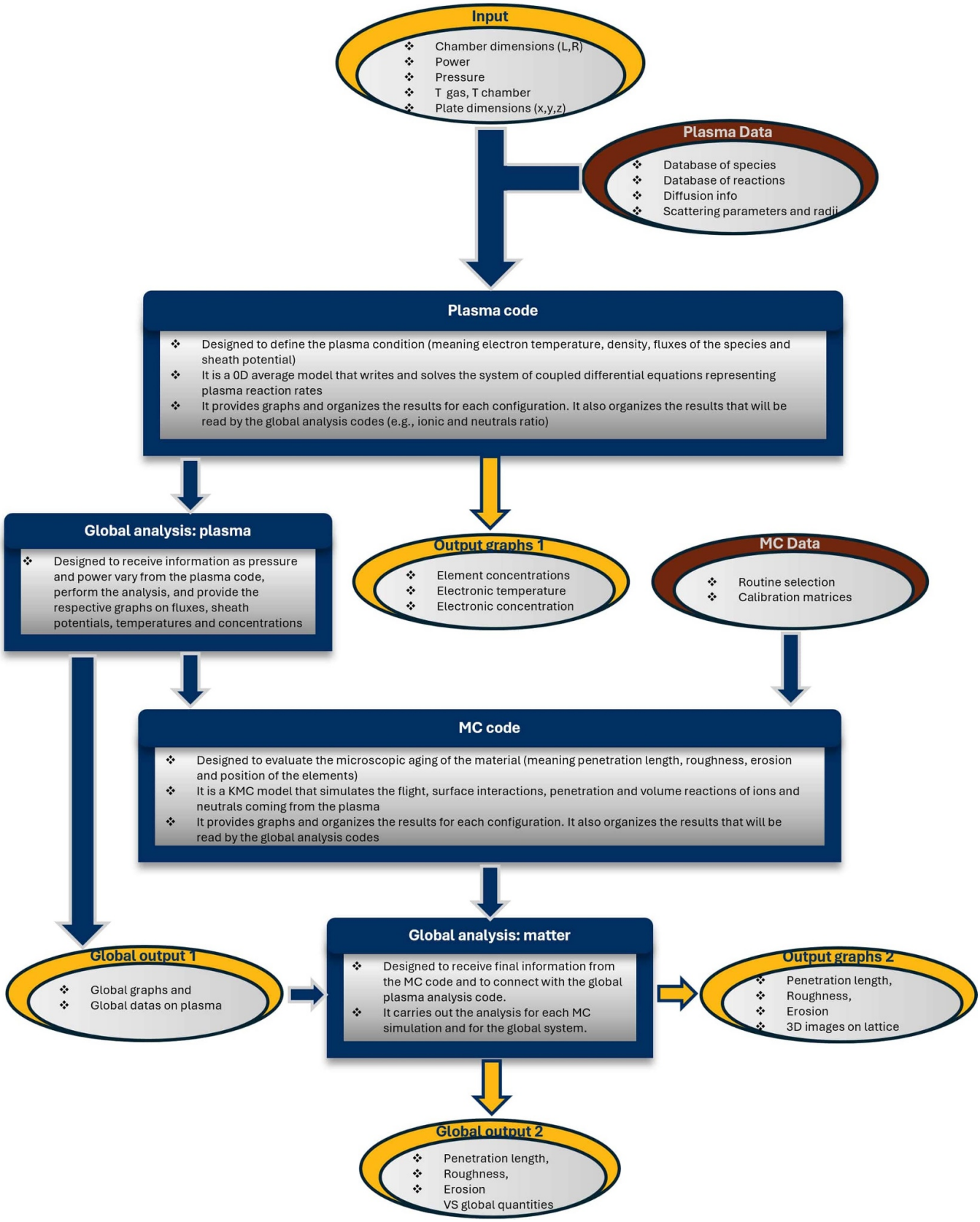

Figure 10. Schematic: coupling between codes.

ORCID iDs

G. Lo Presti https://orcid.org/0009-0003-6382-412X
A. La Magna https://orcid.org/0000-0002-4087-5210

References

[1] EFDA 2012 Fusion electricity—a roadmap to the realisation of fusion energy *Technical Report* (European Fusion Development Agreement) (available at: https://newenergytimes.com/v2/sr/iter/EUROFUSION-EFDA/2012-Roadmap-Excerpt.pdf)
[2] Euro-fusion 2018 European research roadmap to the realization of fusion energy *Technical Report* (Programme Management Unit) (available at: https://euro-fusion.org/wp-content/uploads/2022/10/2018_Research_roadmap_long_version_01.pdf)
[3] Ongena J. and Oost G.V. 2012 *Fusion Sci. Technol.* **61** 3–16
[4] Toschi R. 1997 *Fusion Eng. Des.* **36** 1–8
[5] Nuclear Science & Technology, IAEA 2019 Harnessing energy from nuclear fusion *Technical Report* (available at: www.iaea.org/sites/default/files/19/09/harnessing-energy-from-nuclear-fusion.pdf) (IAEA, Vienna International Centre)
[6] International Atomic Energy Agency 2018 Fusion Energy for Peace and Sustainable Development, IAEA, Vienna (available at: https://nucleus.iaea.org/sites/fusionportal/SiteAssets/18-03925E_BRO_Fusion.pdf)
[7] Abdou M., Riva M., Ying A., Day C., Loarte A., Baylor L., Humrickhouse P., Fuerst T.F. and Cho S. 2020 *Nucl. Fusion* **61** 013001
[8] Ratynskaia S., Bortolon A. and Krasheninnikov S. 2022 *Rev. Mod. Plasma Phys.* **6** 20
[9] Quadling A., Lee W.E. and Astbury J. 2022 *J. Phys. Energy* **4** 030401
[10] Reinhart M. *et al* 2022 *Nucl. Fusion* **62** 042013
[11] Federici G. *et al* 2001 *Nucl. Fusion* **41** 1967
[12] Samuell C.M. *et al* 2014 Hydrogen plasmas and their interaction with fusion-relevant materials *PhD Thesis* The Australian National University
[13] Chromiński W., Ciupiński Ł., Bazarnik P., Markelj S. and Schwarz-Selinger T. 2021 *Mater. Charact.* **174** 110991
[14] Rubel M. 2019 *J. Fusion Energy* **38** 315–29
[15] Marian J. *et al* 2017 *Nucl. Fusion* **57** 092008
[16] Nordlund K., Björkas C., Ahlgren T., Lasa A. and Sand A.E. 2014 *J. Phys. D: Appl. Phys.* **47** 224018
[17] Rapp J. *et al* 2010 *Fusion Eng. Des.* **85** 1455–9
[18] Xu Y. *et al* 2021 *Fusion Eng. Des.* **164** 112198
[19] Song Z., Peng S., Yu J., Ming J., Yuan Z., Qian F. and Guo Z. 2006 *Rev. Sci. Instrum.* **77** 03A305
[20] Tonello E., Formenti A., Alberti G., Uccello A. and Passoni M. 2021 *Nucl. Fusion* **61** 066036
[21] Brezinsek S. *et al* 2017 *Nucl. Fusion* **57** 116041
[22] Wiesen S. *et al* 2015 *J. Nucl. Mater.* **463** 480–4
[23] Bufferand H. *et al* 2013 *J. Nucl. Mater.* **438** S445–8
[24] Bufferand H. *et al* 2015 *Nucl. Fusion* **55** 053025
[25] Reiter D., Baelmans M. and Börner P. 2005 *Fusion Sci. Technol.* **47** 172–86
[26] Samuell C.M. and Corr C.S. 2015 *Plasma Sources Sci. Technol.* **25** 015014
[27] Lieberman M.A. and Lichtenberg A.J. 2005 *Principles of Plasma Discharges and Materials Processing* (Wiley)
[28] Thorsteinsson E. and Gudmundsson J.T. 2009 *Plasma Sources Sci. Technol.* **19** 015001
[29] Wu W. *et al* 2020 *Vacuum* **182** 109744
[30] Hjartarson A., Thorsteinsson E. and Gudmundsson J. 2010 *Plasma Sources Sci. Technol.* **19** 065008
[31] Chiaramonte L., Colombo R., Fazio G., Garozzo G. and La Magna A. 2012 *Comput. Mater. Sci.* **54** 227–35
[32] Campo A., Lombardo S.F., Deretzis I., Garozzo G., Angilella G.G.N. and La Magna A. 2017 *IEEE Trans. Nanotechnol.* **16** 790–7
[33] Kirschner A., Philipps V., Winter J. and Kögler U. 2000 *Nucl. Fusion* **40** 989
[34] Eksaeva A., Marenkov E., Borodin D., Kreter A., Reinhart M., Kirschner A., Romazanov J., Terra A., Brezinsek S. and Nordlund K. 2017 *Nucl. Mater. Energy* **12** 253–60
[35] Borodin D. *et al* 2011 *Phys. Scr.* **2011** 014008
[36] Khan A., De Temmerman G., Lisgo S., Bonnin X., Anand H., Miller M., Pitts R., Schmid K. and Kukushkin A. 2019 *Nucl. Mater. Energy* **20** 100674
[37] Schmid K., Reinelt M. and Krieger K. 2011 *J. Nucl. Mater.* **415** S284–8
[38] Stangeby P. and Elder J. 1992 *J. Nucl. Mater.* **196** 258–63
[39] Osano Y. and Ono K. 2005 *Jpn. J. Appl. Phys.* **44** 8650
[40] Mitchell J., Plimpton S., Thompson A. and Slepoy A. (SPPARKS) 2009 SPPARKS Kinetic Monte Carlo Simulator (available at: https://spparks.github.io/index.html)
[41] MulSKIPS 2019 CNR imm (available at: https://github.com/MulSKIPS/MulSKIPS)
[42] Calogero G., Raciti D., Acosta-Alba P., Cristiano F., Deretzis I., Fisicaro G., Huet K., Kerdilès S., Sciuto A. and Magna A.L. 2022 *npj Comput. Mater.* **8** 36
[43] Lee C. and Lieberman M. 1995 *J. Vac. Sci. Technol.* A **13** 368–80
[44] Burgess A. and Tully J. 1992 On the analysis of collision strengths and rate coefficients *Astron. Astrophys.* **254** 436
[45] Rapp D. and Englander-Golden P. 1965 *J. Chem. Phys.* **43** 1464–79
[46] Yoon J.-S., Song M.-Y., Han J.-M., Hwang S.H., Chang W.-S., Lee B. and Itikawa Y. 2008 *J. Phys. Chem. Ref. Data* **37** 913–31
[47] International Atomic Energy Agency 1992 *Atomic and Plasma–Material Interaction Data for Fusion* vol 2 (International Atomic Energy Agency) (available at: https://www.iaea.org/publications/1837/atomic-and-plasma-material-interaction-data-for-fusion)
[48] Lichtenberg A., Vahedi V., Lieberman M. and Rognlien T. 1994 *J. Appl. Phys.* **75** 2339–47
[49] Lichtenberg A., Vahedi V., Lieberman M. and Rognlien T. 1994 *J. Appl. Phys.* **76** 625 (erratum)
[50] Kim S., Lieberman M., Lichtenberg A. and Gudmundsson J. 2006 *J. Vac. Sci. Technol.* A **24** 2025–40
[51] Thompson J. 1959 Negative ions in the positive column of the oxygen discharge *Proc. Phys. Soc.* **73** 818–21
[52] Boyd R. and Thompson J. 1959 *Proc. R. Soc.* A **252** 102–19
[53] Heckert N.A. NIST 2012 *NIST/SEMATECH e-Handbook of Statistical Methods* (National Institute of Standards and Technology) (https://doi.org/10.18434/M32189)
[54] Patino M., Nishijima D., Tokitani M., Nagata D. and Doerner R. 2020 *Phys. Scr.* **2020** 014070
[55] Chen W., Wang X., Chiu Y., Morgan T., Guo W., Li K., Yuan Y., Xu B. and Liu W. 2020 *Acta Mater.* **193** 19–27
[56] Yin H., Wang J., Guo W., Cheng L., Yuan Y. and Lu G. 2019 *Tungsten* **1** 132–40
[57] Li Y., Zheng Q., Wei L., Zhang C. and Zeng Z. 2020 *Tungsten* **2** 34–71
[58] Zhao Z., Li Y., Zhang C., Pan G., Tang P. and Zeng Z. 2017 *Nucl. Fusion* **57** 086020
[59] Brilliantov N.V. and Pöschel T. 2005 *Chaos* **15** 026108
[60] Kimura T. and Ohe K. 2001 *J. Appl. Phys.* **89** 4240–6
[61] Palmero A., Van Hattum E., Rudolph H. and Habraken F. 2007 *J. Appl. Phys.* **101** 053306